

ULRR

Design rules for antibody delivery by self-assembled block-copolyelectrolyte nanocapsules

Item Type	Article
Authors	Javan Nikkhah, Sousa;Cazade, Pierre-Andre;McManus, Jennifer J.;Thompson, Damien
Citation	Macromolecules 2022, 55, (7), pp. 2383–2397
Publisher	American Chemical Society
Download date	2026-06-16 05:55:14
Item License	https://creativecommons.org/licenses/by-nc-sa/4.0/
Link to Item	https://doi.org/10.34961/researchrepository-ul.24746040

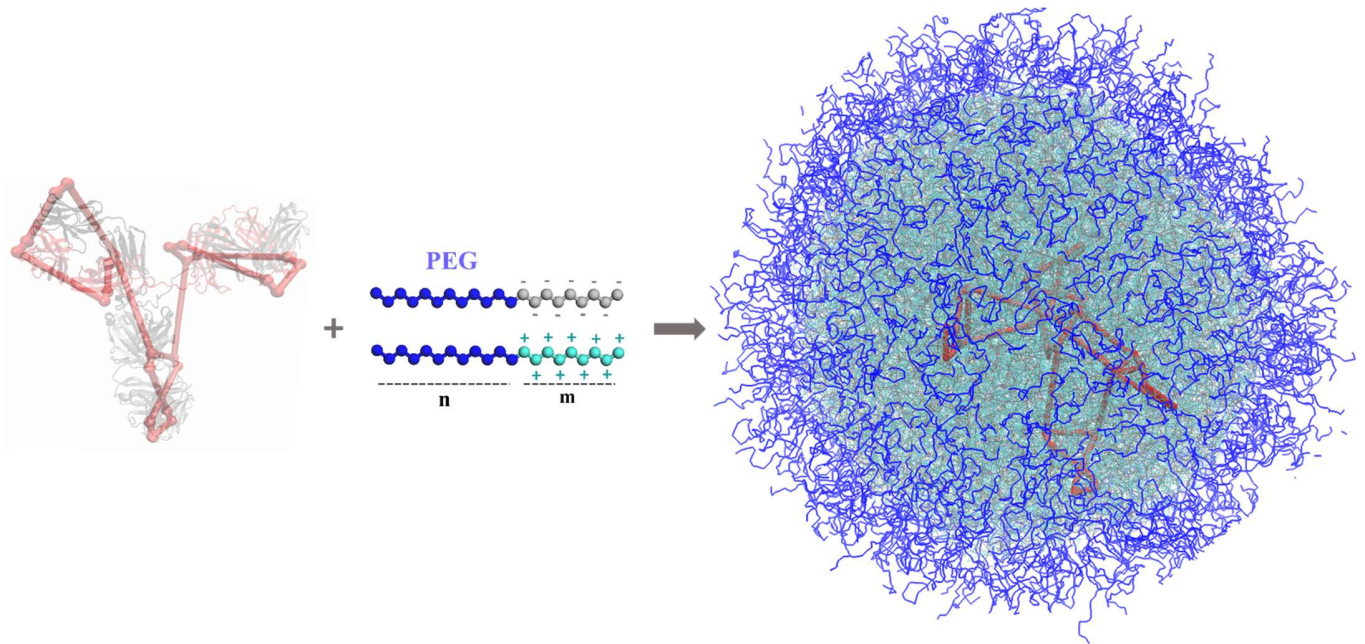
Design rules for antibody delivery by self-assembled block-copolyelectrolyte nanocapsules

Sousa Javan Nikkhah §, Pierre A. Cazade §, Jennifer J. McManus †, Damien Thompson §**

§ Department of Physics, Bernal Institute, University of Limerick, V94 T9PX Limerick, Ireland

† H. H Wills Physics Laboratory, University of Bristol, Bristol BS8 1TL, United Kingdom

Table of Contents



Abstract Monoclonal antibodies (mAbs) are proven biopharmaceuticals for the treatment of chronic illnesses, including cancer, autoimmune, neurodegenerative, and infectious diseases. A fundamental challenge for implementing mAbs in immunotherapy is protecting the protein structure against damage and prolonging its circulation time, which can be achieved using bespoke mAb delivery systems. One promising class of protein carriers is block-copolyelectrolytes (BCPEs, one natural polyelectrolyte grafted to one neutral hydrophilic polymer block) which self-assemble into stable micelles with a compact core of proteins and charged blocks surrounded by a corona of neutral blocks. The simple, biocompatible nano-capsule separates the protein from the outer medium. Here, we design a delivery system for Trastuzumab, an immunoglobulin used to treat breast and stomach cancer. Our proposed mixture of block-copolyanions and block-copolyocations naturally promotes encapsulation through balanced physicochemical interactions in water and is readily tailorable via molecular engineering of the block-copolyelectrolytes. By developing an integrated coarse-grained model to screen different copolyelectrolyte carriers for the specific antibody, we map the carrier assembly and encapsulation mechanism of Trastuzumab in water. Our model identifies the parameters that control encapsulation and forecasts the expected final morphology based on computed phase diagrams of the material over a range of conditions. Specifically for Trastuzumab, we predict that increasing polymer concentration, chain length, and solvent selectivity while decreasing block length ratio will provide more effective BCPE-based mAb delivery. Our efficient computational model can guide future experiments in optimizing copolyelectrolyte-based carrier systems for biopharmaceuticals.

Keywords: Antibody therapy, Protein delivery, Chemotherapy, Copolymer, Polyelectrolyte, Block-copolyelectrolyte, Self-assembly, Aggregation, Coarse-grained molecular modeling.

1. Introduction

Over the past decade, protein therapeutics has become one of the most rapidly growing medical research fields,¹⁻⁵ due to the diverse roles these biopolymers play as building blocks in human physiology.⁶ As drugs, proteins exhibit high target specificity with low toxicity and minimal side effects.^{7,8} These properties make proteins and peptides effective drugs for treating various diseases, including cancer, cardiovascular, and infectious diseases.^{1,2,9-12} Antibodies are large immunoglobulin proteins that can recognize and deactivate their corresponding extracellular antigens,¹³ and are increasingly used in cancer treatment due to outstanding selectivity against the target cells.¹⁴⁻¹⁶ The mechanism of immunotherapy directly targets specific proteins (antigens) uniquely expressed on the surface of cancer cells.¹⁷ These antibodies are classified into two primary types (monoclonal and polyclonal) and have essential roles in the immune response, and therefore disease diagnosis and treatment.¹⁸ Several monoclonal antibodies (mAbs) have been confirmed for clinical use, and many others will continue to be developed as biopharmaceuticals.^{5,13,19-21}

The method of antibody administration is typically parenteral injection since oral delivery systems are challenging to develop for these biologically active compounds.²² However, injected macromolecule drugs can still suffer from enzymatic degradation^{23,24} either at the administration site or in circulation that can further reduce the pharmacokinetics of most classes of proteins.^{23,25,26} Thus, antibody drugs require the development of delivery materials, in this case, protein carrier systems that are efficient both in protein encapsulation and controlled release.²⁷

Polyelectrolyte materials have been investigated as novel platforms to stabilize and deliver small molecule drugs, proteins, and peptides.^{28,29} Polyelectrolyte complexes form through associative phase separation of oppositely charged polymers in an aqueous solution.³⁰ These

charged polymers can be tailored to make completely hydrophilic or compartmentalized assemblies in solution, depending on the chemical attributes, electrostatic interactions, and arrangement of the constituent monomers.^{31,32} Therefore, they are promising candidates for encapsulating large, more complex active pharmaceutical ingredients (APIs) such as proteins and antibodies. However, the assembly mechanism of the complexes must be understood for translation into safe, effective, and reliable end-use technologies.^{33,34}

To create a microphase separated micelle, a block copolymer must be designed with a block of polyelectrolyte and a neutral block to drive self-assembly, combined with an oppositely charged polyelectrolyte to complex with the polyelectrolyte block.³⁵ The neutral block paired with the charged block can be either hydrophilic or hydrophobic,³⁶ which can determine whether the polyelectrolyte complex is located in the core or on the corona of the micelle.³³ Balanced physicochemical interactions, such as hydrogen bonding and hydrophobic contacts, steer the complexation process.^{37,38} In obtaining overall charge neutrality, the concentration of these complexes triggers the formation of the microphase-separated micellar structure, stabilized by the hydrophilic neutral block.³³ Moreover, if the polyelectrolyte block is paired with a hydrophobic neutral block, the block copolymer will form a micelle, even in the absence of the oppositely charged polyelectrolyte, with a hydrophobic core and a corona of polyelectrolyte.³⁹

Various morphologies have been reported, including spherical micelles,^{40,41} worm-like micelles,^{41,42} vesicles,^{43,44} and lamellae.^{45,46} A variety of factors such as temperature,⁴⁶ mixing ratio,⁴⁰ salt concentration,⁴¹ and the net charges, charge distribution, and the concentration of polymers in the system^{46,47} are all thought to influence micelle morphology. For example, supramolecular polyelectrolyte complex micellar assemblies can be fabricated in a system including a block-copolyelectrolyte, synthetic or natural polyelectrolyte such as DNA, and charged

proteins.^{29,48–50} In these supramolecular complexes, the polyelectrolyte blocks act as shielding materials to protect the protein from the outer medium. The neutral blocks prevent macro-aggregation of the complexes, allowing self-assembly of stable polyelectrolyte micelles with tunable size.^{29,51} These protein-containing supramolecular structures have attracted much interest and have been employed for targeted, controlled delivery of therapeutic proteins.^{29,52,53} These and other self-assembled protein carrier materials are discussed in Supporting Note 1.

Computational coarse-grained models can provide unique insight into microstructure to complement experimental studies of the polyion/protein complex formation. In particular, this technique is suitable for learning about assemblies of large proteins such as antibodies which are very large for fully-atomistic models, and hence can be used to understand the morphology and structure of the complex micelle. In this work, we develop a predictive dissipative particle dynamics (DPD)^{54–56} coarse-grained model for a block-copolyelectrolyte-based system to carry Trastuzumab, which is marketed as Herceptin®. Trastuzumab is an IgG1 mAb that is commonly used in the immunotherapy of advanced breast cancers.^{57–59} However, its relatively large size (approximately 150 kD) results in poor pharmacokinetics and weak tumor penetration.⁵⁸ To encapsulate the antibody and so protect it from damage and prolong its half-life in the body, we propose a polyelectrolyte-based platform made from self-assembly of two block-copolyelectrolytes (BCPE) and IgG1. Polyethylene glycol (PEG) acts as the neutral block and in the polyelectrolyte parts of the chains, one of them contains a polycation and the other a polyanion. The models are presented in the Supporting Information in Figure 1.

Self-assembly of BCPE has been widely investigated by different research groups in experimental and simulation studies, for example the Mays^{60,61} and the Pincus^{62,63} groups. In the current study, we introduce this BCPE self-assembly platform as a potential candidate in the

promising field of antibodies therapy. We predict how to tune this platform to achieve high efficacy in protein shielding, towards rational design of highly efficient biomacromolecule delivery systems for, *e.g.*, non-intravenous, oral drug administration.

To the best of our knowledge, this work is the first of its kind to study polyion/Trastuzumab complex aggregate formation using DPD coarse-grained modeling. We use a 24-bead model proposed in ref.⁶⁴ to represent the antibody, where each domain is constituted by two beads, each representing a cluster of hydrophilic and hydrophobic amino acids, respectively.⁶⁴ To find the optimal polyelectrolyte complex-based capsule for the IgG1 antibody, we tune the morphology and structure of the aggregate by varying the polyelectrolyte block properties. Variables include block length ratio, concentration, backbone hydrophobicity, and degree of polymerization. This current work can provide valuable insights and principles to rationally design and engineer novel polyelectrolyte-based protein delivery systems.

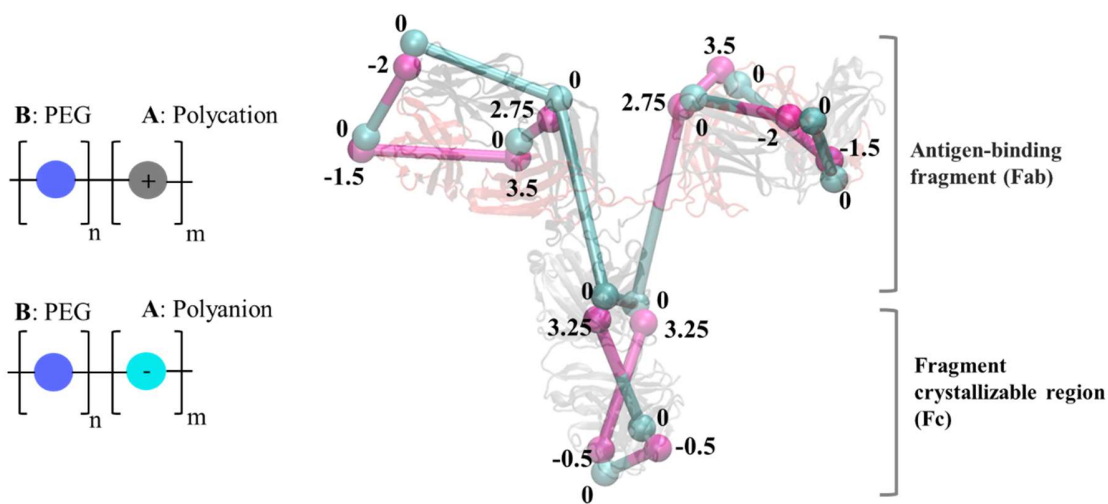


Figure 1. Schematic illustration of the BCPEs (left panel) and the IgG1 antibody (right panel). In BCPE models, PEG (bead type B) and charged beads (bead type A) are presented with navy blue, gray (and aqua blue) colour codes, respectively. The IgG1 model consists of charged (and hydrophilic) and hydrophobic beads as shown with pink and cyan balls, respectively. The values are the beads charges from ref.⁶⁵

2. Methodology

2.1. Simulation details

To enable modeling of multi-antibody self-assembly into stable architectures, we use a force field based on the DPD scheme, a simulation technique intended to bridge the gap between atomistic-level and large-scale analytical network simulations of complex fluids.⁵⁶ We briefly summarise the modeling paradigm below and the coarse-grain forcefield in the Supporting Note 2.

2.2. Computational model and methods

We constructed a simulation box of size $70 \times 70 \times 70 r_c^3$ (where $r_c = 8.43 \text{ \AA}$ (see below), yielding an edge length of 59.01 nm and volume of 205483.45 nm³), which was filled with the IgG1 antibodies and the BCPE molecules, water, counterions with the particle number density $\rho=3$ (where $\rho = \frac{r_c^3}{v_{bead}}$ with r_c and v_{bead} the cutoff radius and bead volume, respectively).⁵⁶ Trastuzumab has a Y-shaped structure, which consists of two light chains and two heavy chains.⁵⁷ The light chains contain two domains each, while each heavy chain has four.¹⁶ We modeled Trastuzumab protein molecules using the coarse-graining method proposed by Dandekar et al.⁶⁴ (at pH = 6) with ~50 amino acids represented by a single spherical bead while preserving the molecule structural features (see Figure 1). According to the proposed method, we modeled the amphiphilic nature of protein molecules by classifying the beads based on charged and hydrophilic (bead type H) and uncharged hydrophobic (bead type N) beads. The charges of the charged and hydrophilic bead (type H) were taken from ref.⁶⁵ and mapped onto the known Trastuzumab molecular structure.⁶⁴
⁶⁶ In this study, a Y-shaped configuration of the IgG1 with a Fab–Fab angle of 36° was modelled using a flexible CG representation⁶⁵ that incorporates the intramolecular interactions between

different domains in the antibody. The simulations were performed at a 10 mg/ml protein concentration corresponding to 8 protein molecules in the simulation cell.

We modeled the polymer chains as fully flexible strings of repulsive beads (of the same size as the solvent and protein beads), kept together by harmonic spring potentials. Two types of polymer chains are denoted, $A_m^+B_n$ and $A_m^-B_n$, where A^+ and A^- represent the positively and negatively charged beads, respectively, and B indicates the neutral water-soluble bead (here, PEG), similar to the method proposed by Šindelka *et al.*⁶⁷ The simulations were performed for four different concentrations of each type of polymer ($\phi_p = \frac{\text{Total beads of polymer}}{\text{Total beads in system}}$) of 0.02, 0.03, 0.04, and 0.05, which corresponded to 258, 386, 515, and 644 molecules of each BCPE in the simulations. Similar concentrations of both types of BCPE are considered in all the simulations. To produce phase diagrams with reasonable high-performance computing cost, the polymer models with the total chain length ($l_t = m$ (polyelectrolyte block length) + n (neutral block length)) values of 40, 60, and 80 were used together with block length ratio ($r_b = \frac{\text{Neutral block len}}{\text{Cha block leng}} = \frac{n}{m}$) values of 0.45, 0.60, 0.78, 1.00, 1.28, and 1.67. While future studies could explore also longer chain lengths for some of these systems, we note that each coarse-grained bead can include more than one polymer repeating unit in its parametrization and so the chains with $l_t = 40-80$ can model very large and complex polymers.

In this study, based on the coarse-graining method of Trastuzumab, one protein bead corresponds to roughly 50 amino acids; thus, a single bead in our model occupies a volume of 200 Å³.⁶⁴ Each water and counterion bead (bead types W and I, respectively) represents ~ 6 water molecules grouped into a bead; W is neutral, and I is charged. Posel *et al.*⁶⁸ showed that applying counterions of the same size as the solvent and polymer beads with smeared electric charge

representing an implicit “mean-field-like” averaging provides a correct treatment of the electrostatic forces. This treatment of the counterions reproduces the conditions existing in polyelectrolyte solutions in experiments by providing the correct numbers of counterions in simulations and ensures a correct treatment of the contribution of ions to the system's entropy. Each PEG bead (bead type B) is composed of about three repeating units.⁶⁹ The mass of the water, counterion, and polymer beads were set to 1, and the protein bead masses, available from ref.⁶⁵, were normalized accordingly.

In our simulations, the modified velocity-Verlet integration algorithm is used to update the coordination of each bead with the integration time step of 0.01. All simulations started from random configurations. Each simulation was conducted with 3×10^6 to 4×10^6 steps using the GNU program DL_MESO⁷⁰, followed by post-processing using LAMMPS (Large-scale Atomic/Molecular Massively Parallel Simulator)⁷¹ to extract physicochemical parameters and obtain predictive design rules for the BCPE-based antibody carrier material. The computed assemblies were visualized using VMD (Visual Molecular Dynamics).⁷²

2.3. Repulsive interaction parameters

First, we clarify the choice of interaction parameters which are listed in Table 1. The self-interactions between like components (a_{ii}) and interactions between the readily soluble components and water, *i.e.*, between counterions and water, are described by $a_{HH} = a_{NN} = a_{AA} = a_{BB} = a_{WW} = a_{II} = a_{WI} = 25$, as is common in DPD studies of polymer solutions and corresponds to the Flory parameter $\chi = 0$.⁵⁶ The interaction parameter between PEG and water is $a_{BW} = 26.3$.⁷³ The choice of other parameters requires more explanation: based on the system studied by Dandekar,⁶⁴ we use a set of parameters that describe IgG1 – IgG1 interactions and interactions between IgG1 and the aqueous solvent at the concentration of 10 mg/ml,

corresponding to values of $a_{NW} = 70$, $a_{HW} = 50$, and $a_{HN} = 50$. We assume IgG1–I and IgG1–PEG interaction parameters are similar to those of IgG1–water ($a_{NI} = 70$, $a_{HI} = 50$, $a_{NB} = 70$ and $a_{HB} = 50$), due to the similarity of the ‘I’ bead with the ‘water’ bead and the high level of hydrophilicity of PEG. These interaction parameters could be refined in future work as experimental data becomes available for a binary system of IgG1–PEG.

A central research question of the present work is, how does the chemical features of the polyelectrolyte influence the morphology and shape of the delivery capsule it assembles around IgG1. Hence, we control the solvent quality for ‘A’ beads by the interaction parameters a_{AW} and a_{AI} , the compatibility between A and B blocks by a_{AB} , and between A blocks and IgG1 by parameters a_{AH} and a_{AN} . For simplicity, we assume $a_{AW}=a_{AI}=a_{AB}$ (as also discussed above for IgG1–water, IgG1–counterion, and IgG1–PEG; $a_{HW}=a_{HI} = a_{HB}$ and $a_{NW}=a_{NI} = a_{NB}$). To control the solvent quality of polyelectrolyte block, a_{AW} is tuned in the range of 25 to 40, which means that the polyelectrolyte backbone affinity for solvent is converted from hydrophilic to hydrophobic.⁷⁴ It should be mentioned that polyelectrolyte interactions with hydrophilic backbones are less critical than those with hydrophobic ones because most polyelectrolytes contain a hydrophobic backbone and dissolve in water only because of the net charges on the chain.⁷⁵ Our coarse-grained model does not depend on mapping the polyelectrolyte models on specific chemical structures. Instead, by varying a_{AW} we provide a comprehensive scan of the role of the polyelectrolyte block solvent selectivity, which yields broad guidelines for the selection and design of suitable polyelectrolyte block chemical structures for future experimental studies. The selected range of a_{AW} (25-40)⁷⁵ includes commonly used polycations such as polylysine,⁷⁶ poly(diallyldimethyl ammonium), poly(4-vinyl pyridine)-C1, quaternized poly(N-trimethylaniline),⁷⁵ poly(4-vinyl pyridine)-C2, poly(dimethylamino)ethyl methacrylate (the DPD

repulsive interaction parameter with water is 35 as reported in ref.⁷⁷) and poly(4-vinyl pyridine)-C3.⁷⁸ The selected range of a_{AW} can also be matched with polyanions, including polyacrylic acid, polystyrene sulfonate, and poly(methacrylic acid).^{77,79} The hydrophilicity of the polyelectrolyte backbone can be modified, and the effect on compatibility with IgG1 beads predicted, by varying the parameters a_{AH} and a_{AN} . Here we vary a_{AN} and a_{AH} in the ranges of 70-55 and 50-35 corresponding to a_{AW} values (25, 30, 35, and 40), which are presented in Table 1.

Table 1. Interaction parameters (a_{ii} and a_{ij}) directing IgG1–BCPE assembly in water at IgG1 concentration of 10 mg/ml, with bead types and parameter values, explained in the text.

	H	N	A	B	W	I
H	25	70	70(65)(60)(55)	70	70	70
N	70	25	50(45)(40)(35)	50	50	50
A	70(65)(60)(55)	50(45)(40)(35)	25	25(30)(35)(40)	25(30)(35)(40)	25(30)(35)(40)
B	70	50	25(30)(35)(40)	25	26.3	26.3
W	70	50	25(30)(35)(40)	26.3	25	25
I	70	50	25(30)(35)(40)	26.3	25	25

3. Results and Discussion

3.1. The theoretical model for polyelectrolyte assembly

Let us here briefly discuss the current concept of the aggregation (complexation) of oppositely charged polyelectrolytes. In general, the morphology of a polyelectrolyte complex resembles a compacted globule, with an interpenetrating internal structure of no apparent long-range order. Although the presence of opposite charges on different chains is essential for aggregation induced by charge neutralization in polyelectrolyte systems, the net contribution of electrostatics to the system's Gibbs free energy is not usually the lead driving force of this process. Regardless of which pair is involved in electrostatic interactions, *i.e.*, two ions, a charged group on the polymer chain and an ion, or two charged groups on the polymer chain, the electrostatic forces can be

balanced through their interactions over a given distance and thus the interaction energy is the same. The main driving force is the entropic term that comprises two main contributions⁸⁰:

(a) "Entropy gain" due to counterion release upon mixing the solution and forming polyelectrolyte aggregates. The extended polyelectrolyte chains collapse to form a compacted globule, driven by the cooperative interaction between two oppositely charged polyelectrolytes. In principle, their topologically connected charged monomers present a stronger affinity to its oppositely-charged analog than to discrete counterions. The solution after polyelectrolyte complexation consists of freely diffusing counterions of both signs and a complex bound by oppositely charged chains.

(b) "Entropy penalty" due to aggregation of polymer chains, which is insignificant for small aggregates but has considerable effect for large one. During complexation, the configurational, translational, and rotational entropies of the polyelectrolyte chains are reduced, the extent of which depends on how compact the chain is within the complex.

However, the electrostatic interactions and the entropy of the liberated ions only influence the aggregation process. In contrast, the formation of specific aggregates (size, shape, and structure) can be steered by other factors such as the amphiphilicity of the PE chains and the incompatibility of chemically different blocks. There are two working hypotheses for BCPE aggregation: (1) If the polyelectrolyte backbone is hydrophilic, the entropy increases due to the liberation of small ions.⁸¹ However, only small aggregates (or only dimers) can be formed because of the hydrophilicity of the small formed aggregates. The process is both entropy-driven (ion liberation) and entropy-controlled (entropy loss of polymer chains in aggregates). In this case, the enthalpy is insignificant because electrostatic forces are balanced, and the aggregation process does not need to minimize the contact between the charged blocks and water. Since IgG1 molecules are not

compatible with the chains (hydrophilic backbone), they cannot influence the aggregation significantly. (2) If the PE backbone is hydrophobic and incompatible with the neutral block, enthalpy plays an important role. Due to incompatibility between the blocks and both water and the hydrophilic neutral blocks, the system attempts to minimize the number of unfavorable contacts between them that results in the formation of large aggregates. However, the self-assembly is driven by a combination of entropy and enthalpy and controlled mainly by entropy, analogous to the aggregation of neutral amphiphilic systems.⁸² Since the IgG1 beads are compatible with the chains (hydrophobic backbone), we propose the IgG1 molecules can catalyze the aggregation due to enthalpy contribution and electrostatic interactions.

3.2. Self-assembly mechanism

In this study, DPD is applied to investigate the physical characteristics of supra-nanoscale assemblies formed between BCPE and IgG1 in water. The BCPE chains are represented as $A_m^+ B_n$ and $A_m^- B_n$ where B indicates the neutral water-soluble bead (here, PEG), and A^+ and A^- represent the positively and negatively charged beads, respectively. The effects of polymer concentration (φ_p), chain length (l_t), block length ratio (r_b), and polyelectrolyte backbone solvent selectivity (a_{AW}) are explored. The self-assembled architectures are mapped by grouping any beads that are within one bead diameter of each other into the same aggregate.⁸³

First, we describe the computed self-assembly mechanism and the dynamic processes for the formation of aggregates in one of the studied systems. Snapshots from a representative IgG1–BCPE capsule containing IgG1, $A_{50}^+ B_{30}$ and $A_{50}^- B_{30}$ ($l_t = 80, r_b = 0.60, \varphi_p = 0.05, a_{AW} = 40$) in water, are presented in Figure 2 to track how aggregates evolve with time. In the beginning, all the molecules are randomly distributed in water (Figure 2a). Then, these randomly distributed

molecules quickly self-assemble into a mixture of small core-shell aggregates (Figure 2b). Subsequently, the small aggregates merged with the neighboring small aggregates and finally formed large core-shell aggregates (Figure 2c-f). In every step of the self-assembly process, all the core-shell aggregates contain a core of oppositely charged polyelectrolyte blocks (A^+ and A^-) and a shell of PEG (Figure 2g). At the end of the simulations, all the IgG1 antibodies are encapsulated within the aggregates (Figure 2g and h). However, some IgG1-free core-shell aggregates are also observed. Additional temporal snapshots and visualization of the aggregate internal structure are provided in the Supporting Information in Figure S1.

Several experimental⁸⁴⁻⁸⁶ and computational^{80,87,88} studies argue that the polyelectrolyte assembly has a strong favorable entropic contribution, which could be driven by the gain in translational entropy of the condensed counterions⁸⁹ that are released when the polyelectrolytes bind together *via* very favorable electrostatic attractions.

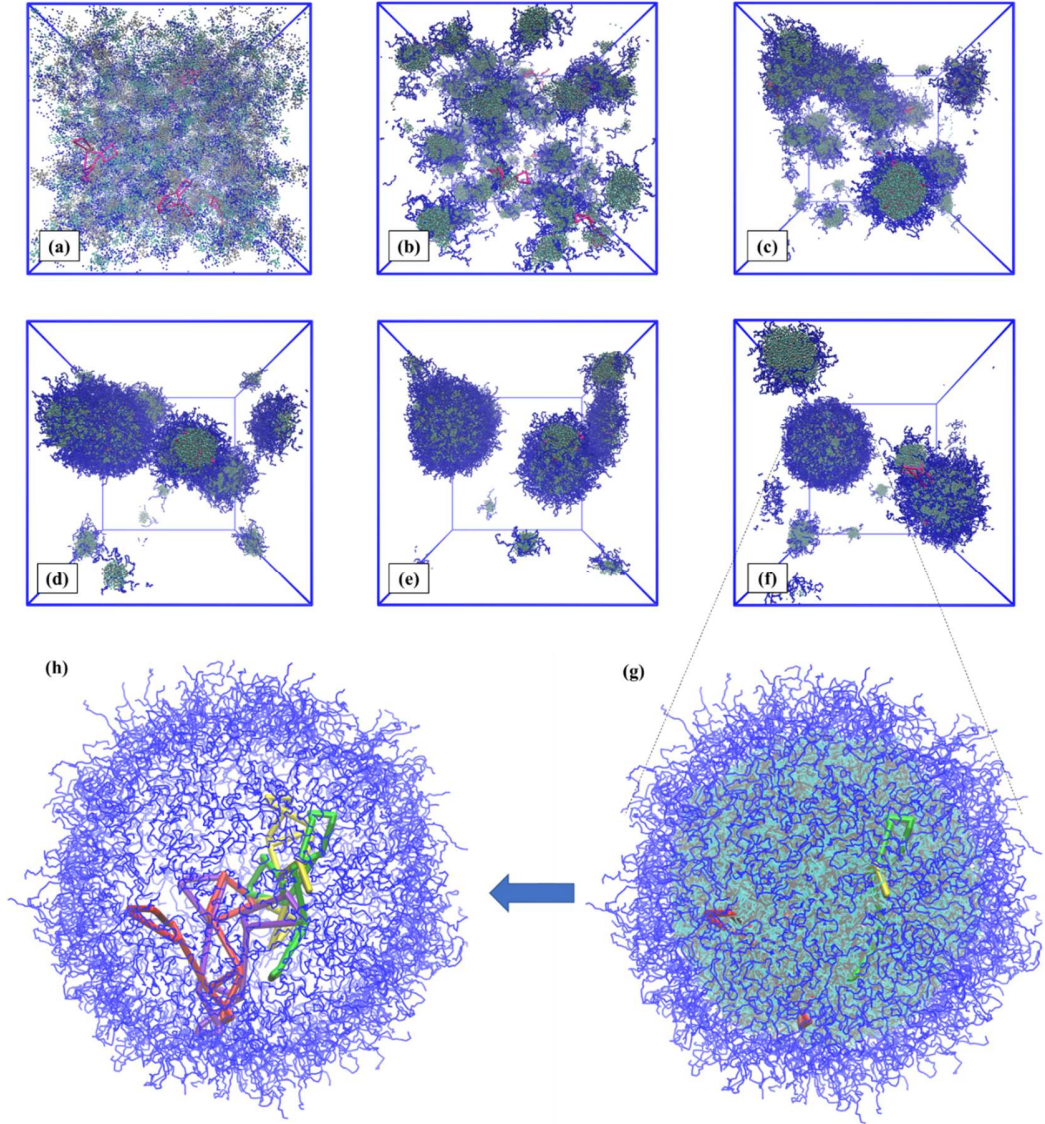


Figure 2. Spontaneous aggregation observed in a simulation consisting of IgG1, $A_{50}^+B_{30}$ and $A_{50}^-B_{30}$ ($l_t = 80$, $r_b = 0.60$, $\varphi_p = 0.05$, $a_{AW} = 40$). The initial random mixture (panel a) evolves during 3.0×10^6 steps into a complex-core-shell aggregate (panel f). The snapshots correspond to simulation timesteps (a) zero, (b) 3×10^4 , (c) 1.2×10^5 , (d) 1.8×10^5 , (e) 9×10^5 , and (f) 3×10^6 steps. Panel (g) shows the magnified picture of a complex-core-shell aggregate encapsulating IgG1. The complex-core region is omitted in panel (h) to indicate the IgG1 molecule inside the aggregate. Gray, cyan, blue, and magenta beads represent A^- , A^+ , PEG, and IgG, respectively. Different color codes for IgG1 molecules (red, violet, green, and yellow) in panels (g) and (h) are to clarify the IgG1 location and configuration in the aggregate. Solvent and counterions are omitted in the visualizations for clarity.

The computed structures track the evolution of the self-assembly of the IgG1–BCPE capsules. Initially, the nuclei for the aggregate formation can form through two mechanisms: (i) oppositely charged polyelectrolyte blocks complexing freely in water, and (ii) polyelectrolyte blocks complexing on the IgG1 charged beads. In mechanism (i), the blocks make small complex-cores covered by PEG-shell at the initial stage of the simulation that act as nuclei for the formation of larger aggregates. In accordance with hypothesis (2) above, the polyelectrolyte backbone hydrophobicity assists the complex formation, as more hydrophobic backbone units shield from water by forming aggregates. On the other hand, in mechanism (ii), the nuclei formation can also start with the complex formation of the polyelectrolyte block and the hydrophobic neutral and charged beads of the IgG1 leading to the IgG1-containing aggregates. Figure S2 of the Supporting Information shows an example of the nuclei formation on the IgG1 and its growth. Besides electrostatic interactions between IgG1 (bead type H) and the polyelectrolyte blocks (bead type A), IgG1 hydrophobicity also has a prominent role in promoting antibody encapsulation through mechanism (ii).

In both cases, the assembly proceeds by free chain adsorption onto nuclei during the early stages (see Figure S2 of the Supporting Information) and terminates in aggregate fusion (see Figure 3). The aggregate fusion in each system can occur as IgG1-free aggregates fuse together, or IgG1-free aggregates fuse with IgG1-containing aggregates, or by fusion of IgG1-containing aggregates. The three mechanisms are shown in Figure 3. All three mechanisms contribute to assembling a useful IgG1-containing aggregate that envelops and protects the antibody from the outer medium. In agreement with hypothesis (2), fusion of IgG1-free aggregates grows the polyelectrolyte matrix large enough to engulf large antibody molecules, which then allows IgG1 encapsulation via fusion with IgG1-containing aggregates. It is worth noting that IgG1–IgG1 complexation that can occur

at the initial steps of the assembly process can result in multi-IgG1-containing aggregates. However, a combination of IgG1–IgG1 complexation in the early stages and the fusion with the fully or partially IgG1-free aggregates in the latter stages is necessary to achieve well-formed multi-IgG1-containing capsules.

As a control, we simulated the same system in the absence of IgG1 molecules to understand the effect of the protein on the self-assembly process. The time evolution snapshots and visualization of the aggregated internal structure of the reference protein-free system are presented in Figure S3. The same mechanism as described above was observed to describe the self-assembly of the reference systems. However, the number of aggregates in the final system is higher in the absence of protein meaning that the IgG1 molecules and their associated aggregate growth mechanisms (an IgG1-free and an IgG1-containing aggregate and two IgG1-containing aggregates) facilitated the self-assembly process.

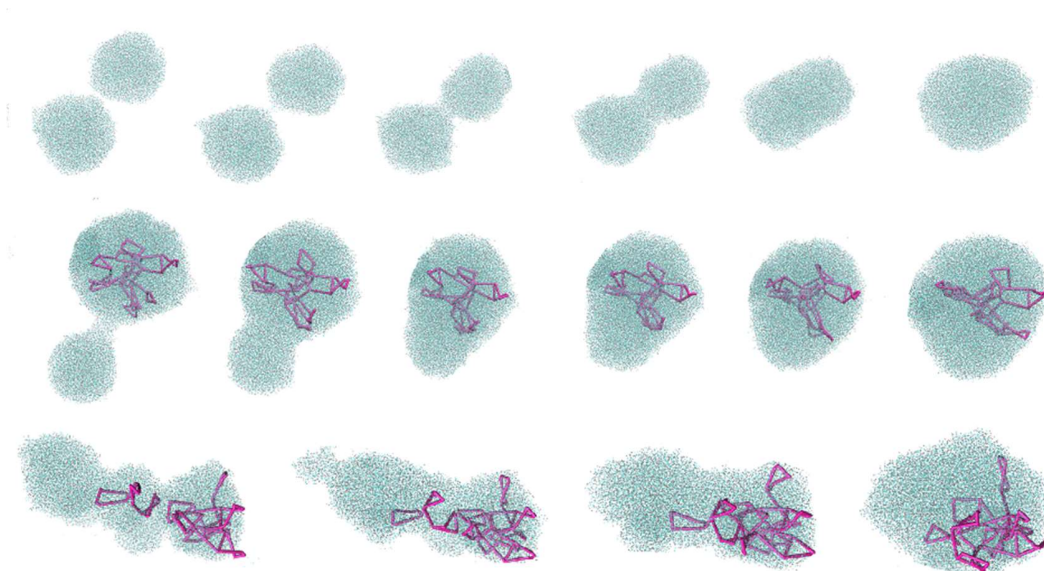


Figure 3. The aggregate growth mechanisms through the fusion of (first row) two IgG1-free aggregates, (second row) an IgG1-free and an IgG1-containing aggregate, and (third row) two IgG1-containing aggregates. Magenta, cyan, and gray beads indicate IgG, A⁻ and A⁺, respectively.

PEG beads are omitted in the visualizations for clarity. PEG beads are omitted in the visualizations for clarity.

3.3. Phase diagram of $A_m^+B_n$, $A_m^-B_n$ and IgG1 in water: Effects of copolyelectrolyte blocks length ratio and polymer concentration

Figure 4 shows the morphological phase diagram of $A_m^+B_n$, $A_m^-B_n$ and IgG1 as a function of r_b and φ_p . The polymer concentration, φ_p , is varied from 0.02 to 0.05, and the block length ratio, $r_b = \frac{n}{m}$, changed from 0.45 to 1.67. For each system studied, we ran three independent simulations starting from different random initial configurations. The time evolution snapshots and visualization of the aggregate internal structure at two points of the phase diagram, including the systems with $\varphi_p = 0.05$ and $\varphi_p = 0.02$ ($r_b = 0.60$, $l_t = 80$, and $a_{AW} = 40$) are provided in the Supporting Information in Figure S1 and S4, respectively.

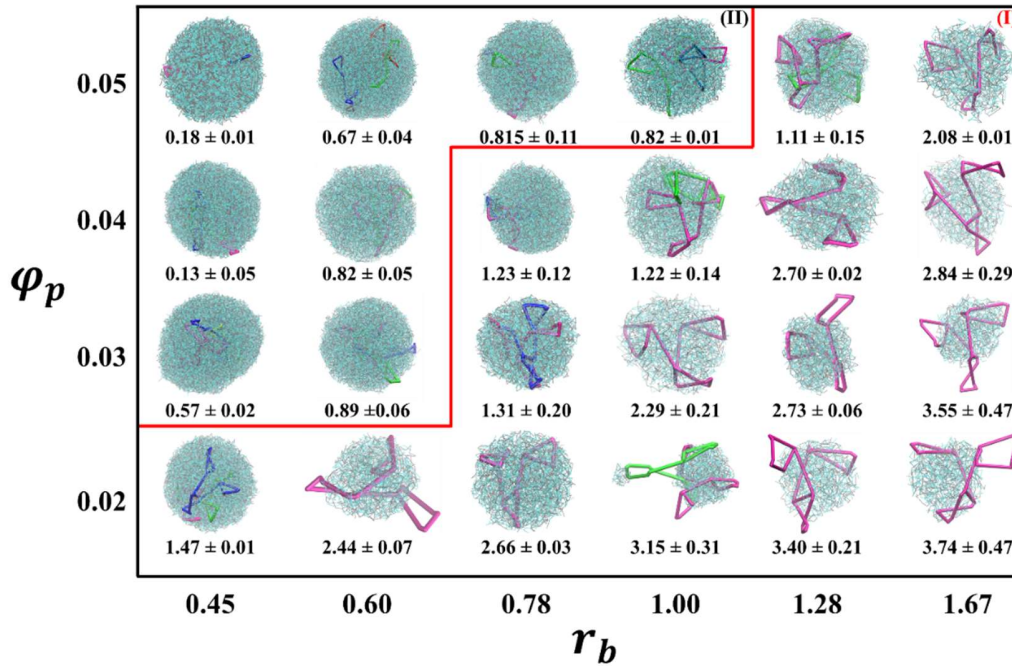


Figure 4. Morphological phase diagram of aggregate formed from IgG1, $A_n^+B_m$ and $A_n^-B_m$ in water as a function of the polymer concentration (φ_p) and block length ratio (r_b) at a fixed $l_t = 80$ and $a_{AW} = 40$. PEG beads are omitted in the visualizations for clarity. The values in the diagram are the average contact between IgG1 and water beads, $C_{\text{IgG1-w}}$, together with standard deviations computed across three sets of simulations. The results of the contact values were averaged across

the sampled data (from the last 20 frames of each simulation. Each frame is 6000 DPD steps apart) of three simulation runs.

To show the effects of r_b and φ_p on IgG1 encapsulation, for each point in the phase diagram, only one of the IgG1-containing aggregates in the system is selected to present. For clarity, only the cores of the selected aggregates are shown. In each of the presented cores, the embedded IgG1 is partially or entirely covered by the polyelectrolyte blocks complexes. In the phase diagram, we identified two main regions according to the level of IgG1 coverage: the cores with partially covered IgG1 (region I) and cores with well-covered IgG1 molecules (region II). Before discussing the assembly regions in more detail, it is essential to note that the simulation system size may affect the size and structural characteristics of the aggregates. To obtain a better understanding of the underlying factors influencing the region transitions in the phase diagram, further analyses of the simulation results were carried out. Average contact number, C_{i-j} between beads i and j per one i bead is measured by calculating the cumulative number of beads j around beads i , out to a contact cutoff distance R_{cutoff} , defined as $C_{i-j} = \frac{\int_0^{R_{cutoff}} \langle n_j(r) \rangle dr}{N_i}$. Here, $n_i(r)$ is the distance r dependent number of beads j around beads i . The contact cutoff, $R_{cutoff} = 1.5r_c$ covers the first maximum of the radial distribution function. N_i is the total number of beads i in the system. Accordingly, the average contact number between IgG1 and water beads per bead of IgG1, C_{IgG1-w} , and between IgG1 and polyelectrolyte beads per bead of IgG1, C_{IgG1-A} were calculated. The calculated contact numbers as a function of r_b and φ_p are presented in Figure 5, and are also shown for convenience in the phase diagram. We used the C_{IgG1-w} values to track the transition between the poorly-protected and well-protected regions. All the points with $C_{IgG1-w} > 1$ are placed in region (I), and region (II) contains all the systems with $C_{IgG1-w} < 1$. The computed contacts were averaged over the sampled data (from the last 20 frames of each simulation) of the

three statistically independent simulation runs and are presented together with their corresponding standard deviations. According to Figures 4 and 5, at a fixed φ_p by increasing r_b , the level of IgG1 coverage by the complex-core decreases, which is confirmed by an increase in $C_{\text{IgG1-W}}$ and a decrease in $C_{\text{IgG1-A}}$. The reasons for this observation are twofold. First, by increasing r_b , the charge of the BCPE chains decreases, leading to a decrease in entropy gain (of the counterion liberation) and electrostatic interaction that hampers complex-core formation and growth (according to hypothesis (1)). Secondly, since bead type A is hydrophobic in all the simulations in this phase diagram, increasing r_b increases the chains hydrophilicity which promotes the formation of the smaller aggregates that cannot embed even a single IgG1 molecule properly (according to hypothesis (2)). Moreover, Figures 4 and 5 show that at a fixed r_b , by increasing the polymer concentration, $C_{\text{IgG1-W}}$ decreases, and $C_{\text{IgG1-A}}$ increases, which represents the improvement in IgG1 encapsulation by the complex-core in the presence of more polymer chains. Since the A block is hydrophobic and incompatible with the B block, increasing the polymer concentration signifies an improvement in the net entropic gain and enthalpy contribution that together facilitate the aggregation.

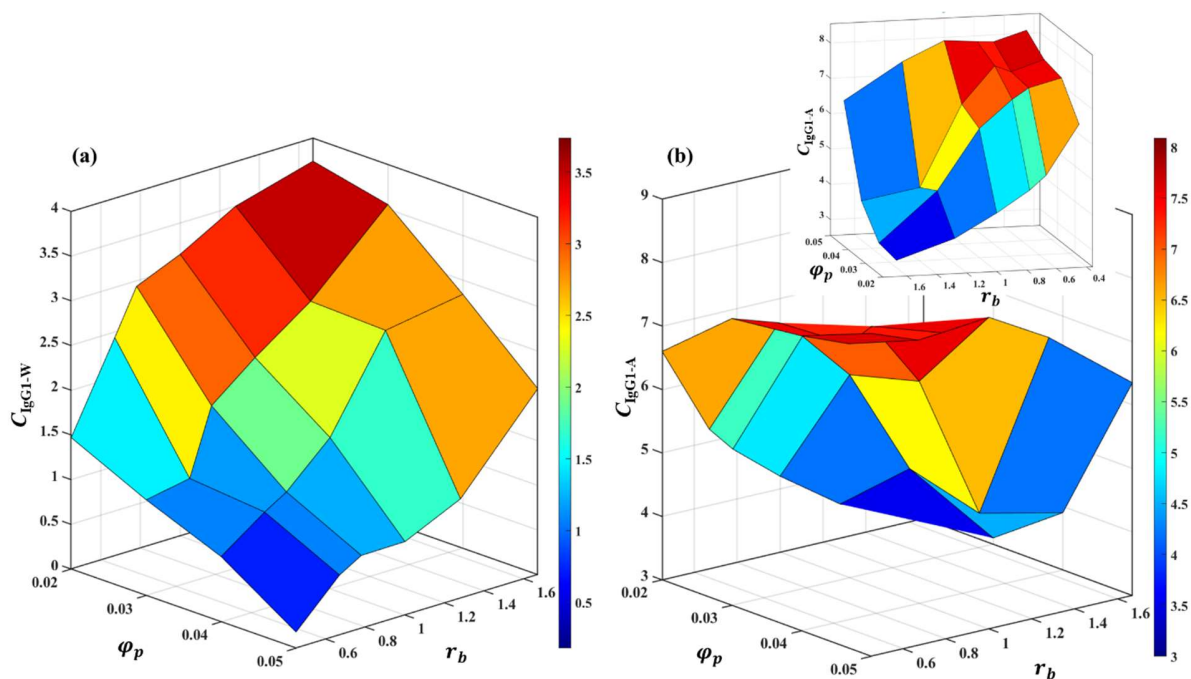


Figure 5. Average contact between IgG1 beads and (a) water beads, and (b) polyelectrolyte block beads (bead type A), per IgG1 bead. **The embedded figure is figure 5b from a different view.**

The radial distribution functions (RDF) between IgG1 and water beads, calculated for systems at two polymer concentrations with varying r_b (see Figure 6), confirms the inferences drawn from the computed contact numbers. The first peak in the RDF (which shows the direct contact between IgG1 and water beads) decreases in height at smaller r_b and almost disappears for the system with the lowest r_b . The smaller values of RDF at lower r_b can be explained by the layered formation of larger aggregates that better protect IgG1 molecules from water by embedding them in their large complex-core. The growth of the aggregate complex-core over time in these systems is presented in Supporting Information Figure S5, confirming the formation of a larger aggregate by decreasing r_b , analogous to the observation in ref.⁵⁰. Moreover, the RDF between the IgG1 and polyelectrolyte blocks (bead type A) presented in Supporting Information Figure S6 also reveals an increase in the IgG1-polyelectrolyte contact by increasing r_b . To understand how the polycation and

polyanion are distributed on the IgG1 molecules, the RDF between the IgG1 and polycation (and polyanion) blocks, for some selected points of the phase diagram are presented in the Supporting Information in Figure S7 and S8. No significant difference between the RDF curves (IgG1-Polycation and IgG1-Polyanion) is observed, meaning a random interpenetrating of the polyanion, polycation blocks, and IgG1 molecules took place in the self-assembly process without apparent long-range order.

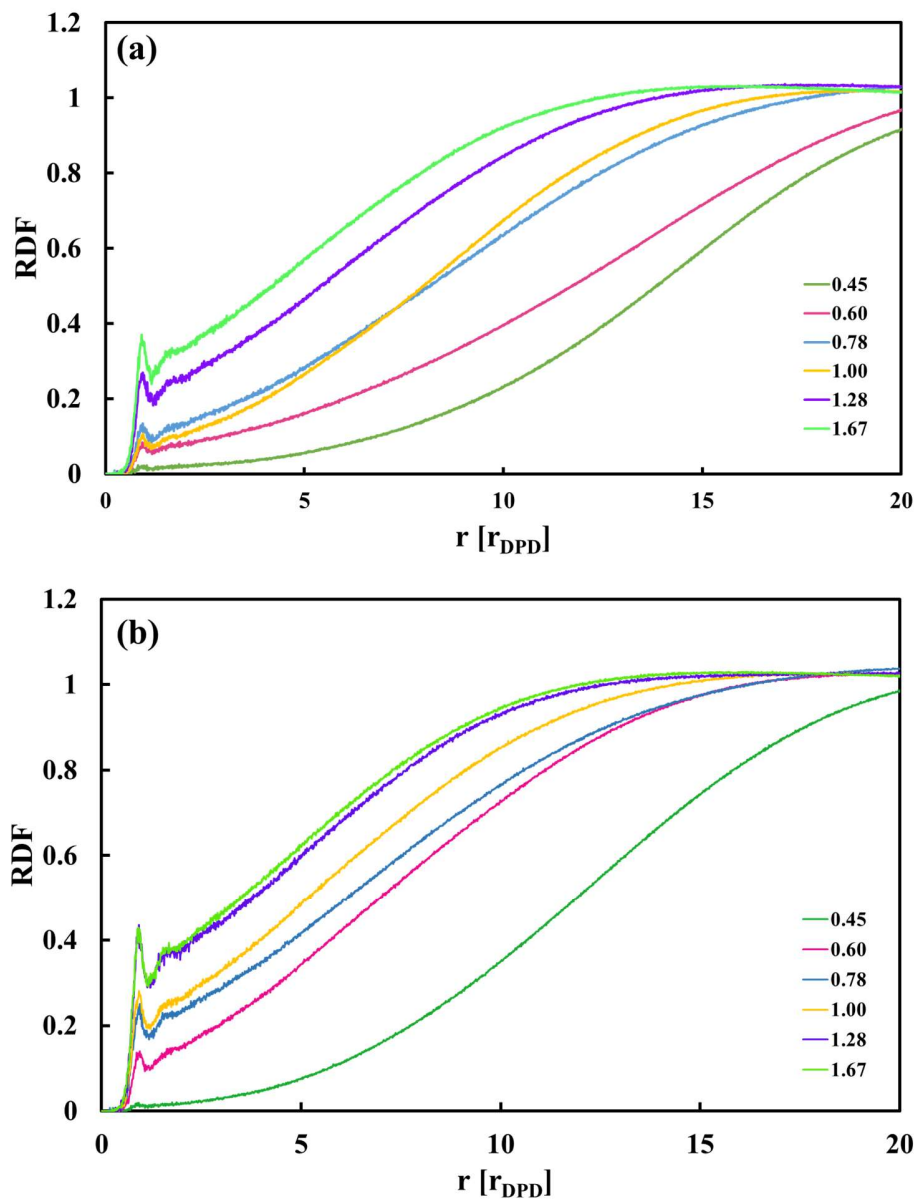


Figure 6. Radial distribution function between the IgG1 and water beads for the systems with different r_b (0.45, 0.60, 0.78, 1.00, 1.28, 1.67), (a) $l_t = 80$, $a_{AW} = 40$ and $\varphi_p = 0.05$, and (b) $l_t = 80$, $a_{AW} = 40$ and $\varphi_p = 0.04$. RDF data analysis is based on the last 20 frames of the simulations. In the legend, the values are r_b .

Figure 7 summarizes the quantitative data derived from three independent simulations of the systems with polymer concentrations of 0.05 and 0.04. Initially, most of the polymer chains and IgG1 are free; at the end of the simulation, essentially all of the chains and IgG1 molecules

are incorporated into a few large aggregates. This behavior is expected since the polyelectrolyte block backbone and the IgG1 molecules (at the studied IgG1 concentration) are hydrophobic. In the final aqueous solvent, the lack of a protective coating makes fusion and coagulation likely for each aggregate collision. The final experimental system would presumably form one or a few large aggregates, the size of which would depend on the polymer concentration, chain length, block length ratio, and polymer-solvent selectivity.

As illustrated in Figure 7, the general shape of the aggregate number curves can be understood by accounting for the competition between aggregate formation and the growth of existing aggregates. Initially, most of the polymer chains and IgG1 are free; thus, the probability that a polymer chain (or IgG1 molecules) encounters another polymer chain (or IgG1 molecules) rather than an aggregate is high, and the number of aggregates increases. As more aggregates form and grow by addition of a single chain or IgG1 molecule, the decrease in the concentration of free polymer chains (or IgG1 molecule) reduces the new aggregate formation rate. Finally, the fusion of existing aggregates into larger ones decreases the total number of aggregates (see Figure 3 for the mechanisms of the aggregate fusion).

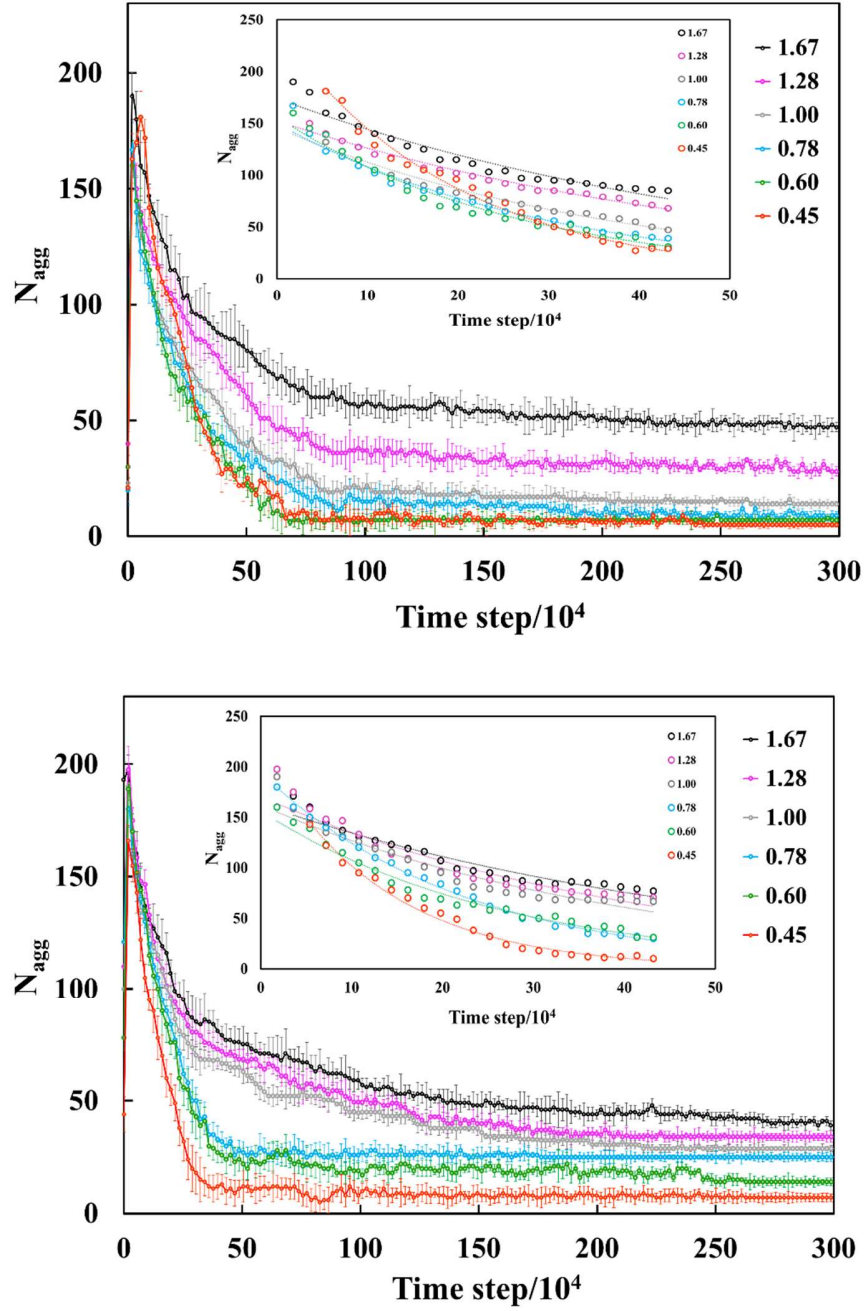


Figure 7. The time evolution of the number of aggregates (N_{agg}) for the systems with different r_b (0.45, 0.60, 0.78, 1.00, 1.28, 1.67), (a) $l_t = 80$, $a_{AW} = 40$ and $\varphi_p = 0.05$, and (b) $l_t = 80$, $a_{AW} = 40$, and $\varphi_p = 0.04$. The insets show fits to the exponential model of the number of aggregates for times between t_0 and 43×10^4 , and at different simulation steps for different block length ratios, r_b .

The results were averaged across the three simulation runs, and the standard deviations were plotted as error bars on the data. In the legend, the values are r_b .

To assess the kinetics of aggregate formation, we estimated the times associated with this process. Although there are many possibilities, here we define the aggregate formation time τ_c by fitting the number of aggregates (N_{agg}) curve versus time after the maximum to the expression $N_{agg}(t) = De^{-\frac{t}{\tau_c}}$, in which t and τ_c are time and characteristic time, respectively. We fit the data from the time at the maximum point until a time of 43×10^4 . Figure 7 shows the fitting curves of the systems with a polymer concentration of 0.04 and 0.05. Table 2 summarizes the characteristic times associated with all the simulations. At a fixed r_b , the lower polymer concentrations generally lead to longer characteristic times, consistent with the decreased probability of interactions when concentration is reduced. On the other hand, at a constant polymer concentration, increasing r_b gives longer characteristic time because we are decreasing the polyelectrolyte block length, which is one of the fundamental driving forces of antibody encapsulation (according to the working hypothesis).

Table 2. Characteristic time (in DPD unit) of the aggregate formation process as a function of φ_p and r_b at a fixed $l_t = 80$ and $\alpha_{AW} = 40$. The values in parentheses are the coefficients of determination of fitting, R^2 .

$\varphi_p \backslash r_b$	0.45	0.60	0.78	1.00	1.28	1.67
0.02	4.25×10^3 (0.990)	4.50×10^3 (0.994)	4.50×10^3 (0.965)	6.00×10^3 (0.955)	6.25×10^3 (0.985)	6.50×10^3 (0.984)
0.03	4.15×10^3 (0.980)	4.25×10^3 (0.990)	5.25×10^3 (0.968)	5.75×10^3 (0.965)	6.00×10^3 (0.980)	6.00×10^3 (0.935)
0.04	2.25×10^3 (0.990)	2.50×10^3 (0.980)	3.50×10^3 (0.997)	5.00×10^3 (0.937)	5.00×10^3 (0.910)	5.00×10^3 (0.944)
0.05	2.00×10^3 (0.985)	2.00×10^3 (0.979)	3.33×10^3 (0.972)	3.33×10^3 (0.963)	5.00×10^3 (0.963)	5.00×10^3 (0.946)

3.4. Phase diagram of $A_m^+B_n$, $A_m^-B_n$ and IgG1 in water: Effects of copolyelectrolyte blocks length ratio and the polyelectrolyte block solvent selectivity

To systematically investigate the morphologies self-assembled from $A_m^+B_n$, $A_m^-B_n$, and IgG1 in selective solvents for the copolyelectrolyte blocks (bead type A) and with different block length ratios of BCPE, a morphological phase diagram was constructed. The phase diagram is displayed in terms of the interaction parameters a_{AW} and r_b at a fixed $\varphi_p = 0.05$ and $l_t = 80$ (see Figure 8).

To study the solvent selectivity in addition to varying a_{AW} , the interaction parameter between the polyelectrolyte and the counterion (a_{AI}), the interaction parameter between the polyelectrolyte and PEG (a_{AB}), and the interaction parameters between the polyelectrolyte and IgG1 (a_{AN} and a_{AH}) were also changed correspondingly (according to Table 1). The time evolution snapshots and a visualization of the aggregate internal structure of one of the phase diagram points ($l_t = 80$, $r_b = 0.45$, $\varphi_p = 0.05$, and $a_{AW} = 35$) are provided in the Supporting Information in Figure S9. We define the regional boundaries in the phase diagram as follows: (1) making a separation between aggregate-containing and solution-containing regions, and (2) making a separation between the different subregions in the aggregate-containing area based on the values of C_{IgG1-W} (as discussed in Section 3.3). Three main regions were specified in the phase diagram, accordingly. In region (I), only slight aggregation is detected due to the hydrophilicity of the copolymer chains and their incompatibility with the IgG1. In region (II), the aggregates formed, but IgG1 was only partially encapsulated. In this region, the nucleation and aggregate formation is the consequence of increasing a_{AW} (increasing the surface tension between the polyelectrolyte backbone and water). However, increasing r_b acted as a controlling factor that limited the assembly of the envelope. In region (III), the IgG1 molecules are completely encapsulated in the complex-cores with lower

values of $C_{\text{IgG1-w}}$. Our model shows how increasing a_{AW} and decreasing r_b can reinforce the role of the mechanisms of nucleation (mechanisms (i) and (ii)) and aggregate fusion in the self-assembly process.

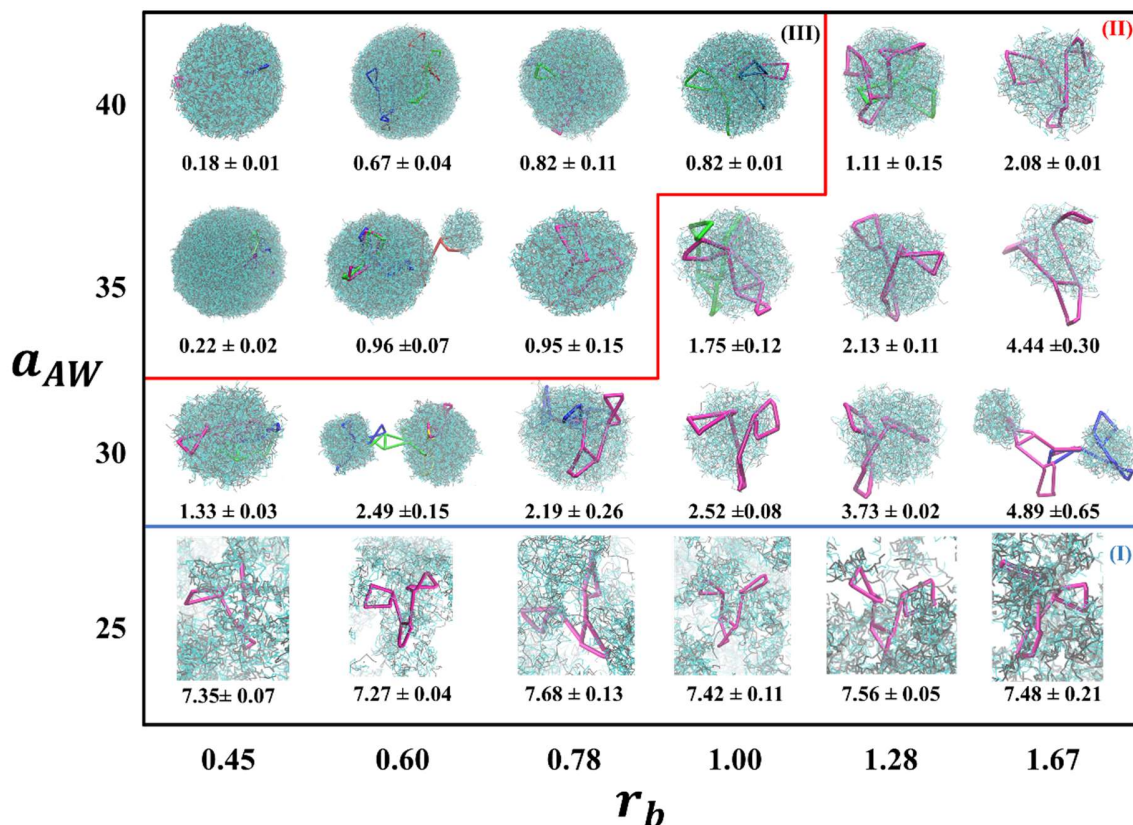


Figure 8. Morphological phase diagram of aggregate formed from IgG1, $A_m^+ B_n$ and $A_m^- B_n$ in water as a function of the polyelectrolyte block solvent selectivity (a_{AW}) and block length ratio (r_b) at a fixed $l_t = 80$ and $\varphi_p = 0.05$. The values in the diagram are the average contact between IgG1 and water beads, $C_{\text{IgG1-w}}$. The results of the contact values were averaged across the sampled data (from the last 20 frames of each simulation. Each frame is 6000 DPD steps apart) of three simulation runs.

The observations in the phase diagram confirm the working hypotheses. The values in the phase diagram show the average contact number between IgG1 and water beads per bead of the IgG1. According to the contact number data (see Figure S10 of the Supporting Information), the best protection of IgG1 (the most effectively buried protein with the lowest contact with water)

happens at the lowest r_b and the highest a_{AW} . In Figure 8 and Figure S10 we show that at a fixed r_b , increasing a_{AW} leads to a decrease in the IgG1 contact with water. Similarly, at a fixed a_{AW} , the larger complex-core can better surround and protect the IgG1 molecules simply by decreasing r_b .

The RDFs between IgG1 and water and between IgG1 and polyelectrolyte blocks beads are presented in Figure 9 as a function of a_{AW} , for three systems with different r_b , 0.45, 0.78, and 1.28. The RDFs of the rest of the systems are presented in Supporting Information, Figure S11. It can be seen in Figure 9 that at a fixed r_b , by increasing a_{AW} , the RDF value of IgG1–W decreases while that of IgG1–A increases, which confirms the results of the IgG1 average contact number with water. Moreover, the early plateau in the RDF curves for the systems with $a_{AW} = 25$, with the RDF values around 1, confirms that the aggregation could take place only slightly in those systems (region (I), which agrees with hypothesis (1)). Increasing the RDF value of IgG1-A by increasing a_{AW} , *i.e.*, increasing probability of finding A beads in the vicinity of IgG1, confirms the better protection of IgG1 molecules by the complex-cores.

To investigate the kinetics of the aggregate formation, we computed the time evolution of the number of aggregates (N_{agg}) for the systems with different polyelectrolyte block solvent selectivity (see Supporting Information, Figure S12), as derived from three independent simulations. Since significant aggregation was not observed for the system with $a_{AW}=25$, we did not include it. The results reveal that at a fixed block length ratio, r_b , at each step of the simulation, higher a_{AW} values for the polyelectrolyte produces lower N_{agg} . This observation quantifies the effect of hydrophobicity of the polyelectrolyte backbone as one of the driving forces for nucleation, aggregate formation, growth, and aggregates fusion. To complete our study on the kinetics of the aggregation, we also calculated the characteristic time, τ_c (Table 3). As discussed previously,

increasing r_b slows the assembly, *i.e.*, increases τ_c . On the other hand, at a fixed r_b , increasing a_{AW} (increasing the incompatibility between IgG1 and water), promotes aggregate formation, yielding smaller τ_c (confirming the working hypothesis).

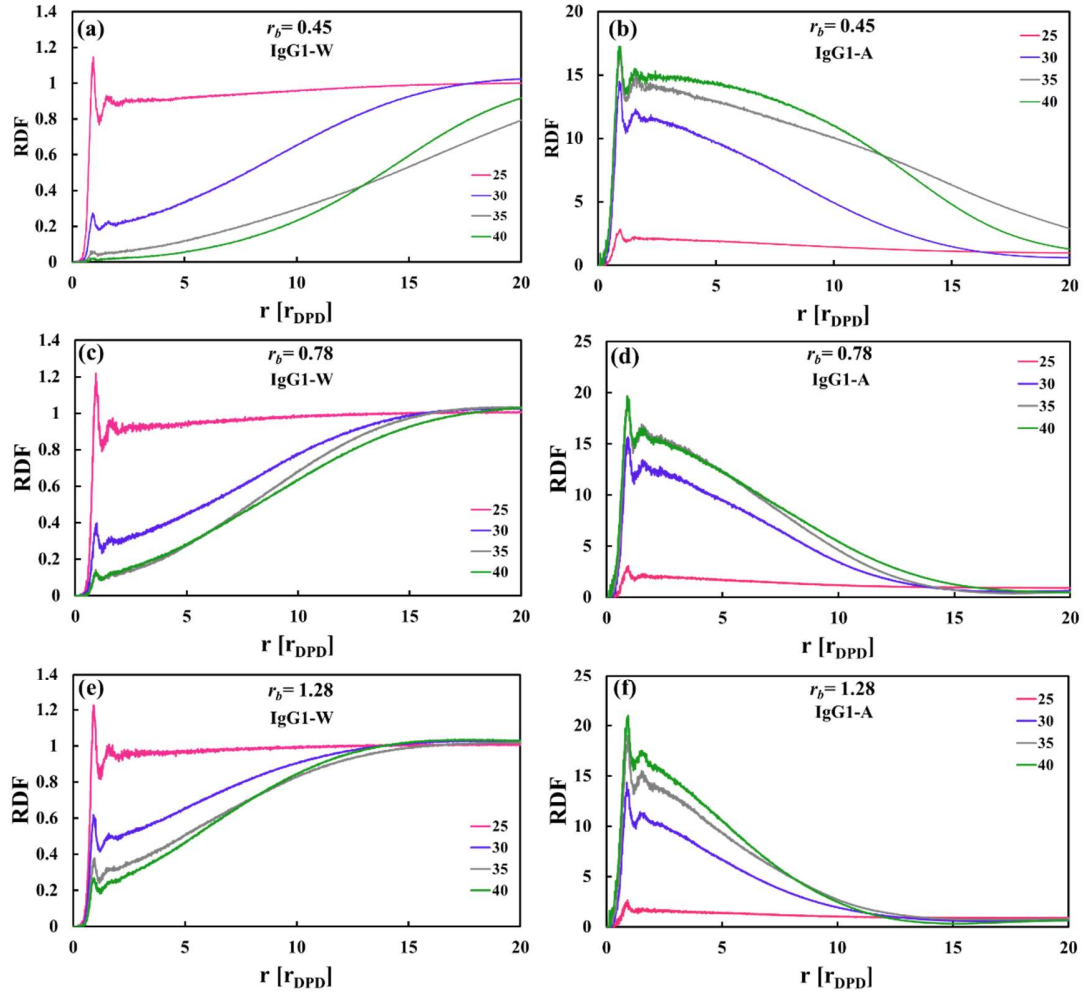


Figure 9. Radial distribution function between the IgG1 and water beads for the systems with different a_{AW} (25, 30, 35, 40), $l_t = 80$, $\varphi_p = 0.05$, and (a) $r_b = 0.45$, (c) $r_b = 0.78$, and (e) $r_b = 1.28$. Radial distribution function between the IgG1 and the polyelectrolyte beads (type A) for the systems with different a_{AW} (25, 30, 35, 40), $l_t = 80$, $\varphi_p = 0.05$, and (b) $r_b = 0.45$, (d) $r_b = 0.78$, and (f) $r_b = 1.28$. RDF data analysis is based on the last 20 frames of the simulations. In the legend, the values are a_{AW} .

Table 3. Characteristic time (in DPD unit) of the aggregate formation process as a function of a_{AW} and r_b at a fixed $\varphi_p = 0.05$ and $l_t = 80$. The values in parentheses are the coefficients of determination of fitting, R^2 .

$a_{AW} \backslash r_b$	0.45	0.60	0.78	1.00	1.28	1.67
30	8.20×10^3 (0.968)	8.50×10^3 (0.977)	8.75×10^3 (0.988)	9.50×10^3 (0.945)	9.50×10^3 (0.970)	1.00×10^4 (0.902)
35	3.25×10^3 (0.980)	4.50×10^3 (0.975)	4.75×10^3 (0.987)	5.00×10^3 (0.957)	5.00×10^3 (0.980)	5.00×10^3 (0.977)
40	2.00×10^3 (0.985)	2.00×10^3 (0.979)	3.33×10^3 (0.972)	3.33×10^3 (0.963)	5.00×10^3 (0.963)	5.00×10^3 (0.946)

3.5. Phase diagram of $A_m^+B_n$, $A_m^-B_n$ and IgG1 in water: Effects of copolyelectrolyte block length ratio and chains length

Our model also tracked how the polymer degree of polymerization and block length ratio can impact the aggregate morphology. The morphological phase diagram with block length ratio, r_b , and chains length, l_t , is plotted in Figure 10. It can be observed from the diagram that at a fixed r_b , increasing the chain length from 40 to 80 leads to a decrease in the average contact between IgG1 and water. We suggest two possible reasons for this observation. Decreasing the chains solubility in water by increasing the degree of polymerization, while on the other hand by increasing the chain length and having longer polyelectrolyte blocks, the formation of the aggregates with larger complex-cores can better desolvate IgG1 molecules (improving the aggregate growth mechanisms). The average size of the aggregate complex-core versus time corresponding to the systems with $r_b = 1.67$ ($a_{AW} = 40$, and $\varphi_p = 0.05$) in the phase diagram are presented in Supporting Information Figure S13. The curves map out, at a constant r_b , the growth in complex-core size with an increase in the chains degree of polymerization.

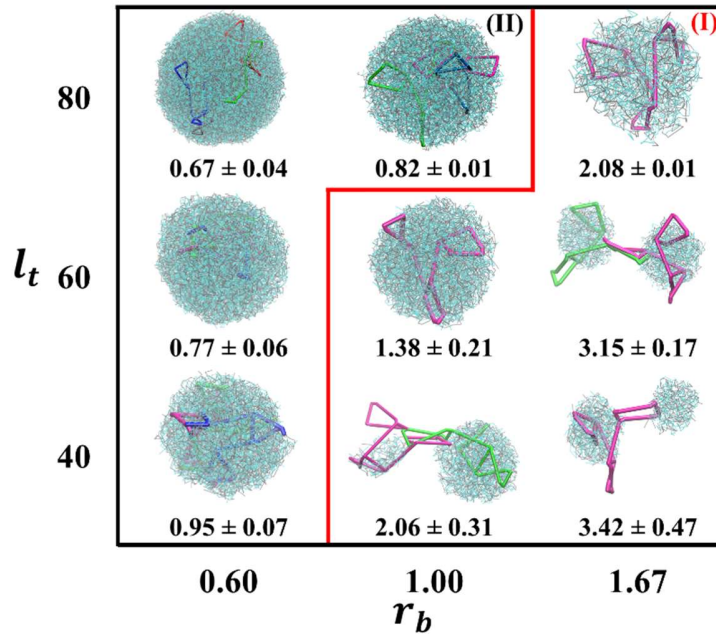


Figure 10. Morphological phase diagram of aggregate formed from IgG1, $A_n^+B_m$ and $A_n^-B_m$ in water as a function of the polymer chain length (l_t) and block length ratio (r_b) at a fixed $\varphi_p = 0.05$ and $a_{AW} = 40$. PEG beads are omitted in the visualizations for clarity. The values in the diagram are the average contact between IgG1 and water beads. The contact values were averaged together across the sampled data (from the last 20 frames of each simulation. Each frame is 6000 DPD steps apart) of the three simulation runs, and the standard deviations in these amounts were calculated accordingly.

As can be seen in the phase diagram, based on the values of C_{IgG1-w} , there are two main regions detected: in the region (I), IgG1 molecules are not coated properly by the complex-cores, as evident from both the morphologies and IgG1 average contact with water. In region (II), the core-shell aggregates with appropriately encapsulated IgG1 molecules in the complex-core area are observed. In the current modeling system, we could predict how tuning a combination of these two effective factors (r_b and l_t) can synergistically impact the IgG1 encapsulation. The RDF between IgG1 and water beads for all points of the phase diagram is presented in the Supporting Information, Figure S14. The results show that at a fixed polymer concentration, φ_p , and a fixed block length ratio, r_b , the RDF values between IgG1 and water beads decrease with an increase of

the polymer chain length, which confirms the results of average contact with water in Figure 10. The results of RDF between IgG1 and the polyelectrolyte blocks (bead type A) are presented in the Supporting Information, Figure S15, confirming the increase in the RDF values by increasing l_t , at fixed polymer concentration and block length ratio. Finally, the RDF curves between IgG1 and polycation (and polyanion) blocks presented in Figure S16 show a random interpenetrating structure of the charged blocks on the IgG1 molecules (as discussed in Section 3.3).

4. Conclusions

Through a systematic, extensive scan of the physicochemical parameters of protein-polyelectrolyte assembly using a bespoke computational model, we identified the key design principles to create an effective drug delivery vehicle to fully encapsulate the monoclonal antibody, Trastuzumab (IgG1), using a block-copolyelectrolyte (BCPE) material. We predicted phase diagrams and self-assembly mechanisms in a three-component mixture of block-copolycation, block-copolyanion, and IgG1 in water using DPD simulations. The BCPE chains were composed of a neutral solvophilic block of polyethylene glycol (PEG) and a charged block. Keeping a fixed IgG1 concentration, we investigated the effect of four important systems parameters on the self-assembly and encapsulation of IgG1, including block length ratio (r_b), polymer concentration (ϕ_p), polyelectrolyte block solvent selectivity (a_{AW}), and polymer chain length (l_t). We showed that in particular conditions, the three-component mixture self-assembled into core-shell aggregates. The core is composed of the polyelectrolyte complex that is covered and stabilized with a shell of PEG. In each system, two types of aggregates were observed, IgG1-free and IgG1-containing aggregates. The results show that in IgG1-containing aggregates, the IgG1 molecules are placed in the complex-core area. The self-assembly started by quick aggregation of randomly distributed molecules into a mixture of small core-shell aggregates. The small aggregates could

form either freely in water or on charged sites of IgG1. Therefore, the small aggregates fused into the neighboring small aggregates and finally formed large core-shell aggregates. We observed three aggregates fusion mechanisms that led to aggregate growth, including the fusion of two IgG1-free aggregates, one IgG1-free and one IgG1-containing aggregates and, the fusion of two IgG1-containing aggregates.

The assembly response and transitions were also studied by providing morphological phase diagrams in terms of the system parameters. In the first phase diagrams, we observed the effect of varying r_b (block length ratio) and φ_p (polymer concentration) on the morphology of the aggregates and average contact between IgG1 and water. Our main finding is that, at a fixed polymer chain length and solvent selectivity, better encapsulation of IgG1 occurred when we decreased r_b and increased φ_p . The second morphological phase diagram, which was as a function of r_b and a_{AW} (polyelectrolyte block solvent selectivity), showed that regardless of the value of r_b , to form aggregates, a_{AW} should be sufficiently large. According to this phase diagram, increasing a_{AW} besides decreasing r_b made an improvement in the IgG1 encapsulation. We also studied the effect of simultaneously varying r_b and l_t (the polymer chain length) via the third phase diagram. We observed that decreasing r_b and increasing l_t together promoted the creation of larger aggregates that were able to enclose single or several IgG1 molecules in their complex-cores.

By varying the system parameters, we identified the ranges in which properly IgG1-protecting aggregates assemble. The work revealed some important practical guidelines for IgG1-BCPE assembly formation. Our simulations predict that increasing solvophobicity of the polyelectrolyte blocks backbones, polymer chain length, and polymer concentration and decreasing the block length ratio will create optimal conditions for efficient encapsulation of IgG1 macromolecules inside the proposed BCPE-based delivery system. The DPD based computational

framework we developed can be easily tuned for the design of other types of biopharma carrier systems with different biomolecules and any current or future self-assembling nanostructures in solution.

The structural transitions presented here, and their relation to direct polymer chemistries *via* the interaction parameters, provide guidelines for the IgG1-BCPE assembly. However, naturally, for designed polymeric systems, other practical factors such as the atomic-scale chemistry of the hydrophilic block, charge fraction, BCPEs stoichiometry, the presence of buffers and other environmental molecules, and temperature will all influence the assembly. As a final point, to make the proposed system applicable as a carrier for IgG1 particularly for treatment of stomach cancer, it would be interesting to explore and design future BCPE-based delivery systems that are particularly robust at low pH.

Associated Content Current state of the art in experiments and modeling of protein encapsulation by organic self-assemblies. Time evolution formation of the system includes IgG1, $A_{50}^+B_{30}$ and $A_{50}^-B_{30}$ ($l_t = 80, r_b = 0.60, \varphi_p = 0.05, a_{AW} = 40$). Visualization of enveloping of IgG1. Time evolution formation of the system includes $A_{50}^+B_{30}$ and $A_{50}^-B_{30}$ ($l_t = 80, r_b = 0.60, \varphi_p = 0.05, a_{AW} = 40$). Time evolution formation of the system includes IgG1, $A_{50}^+B_{30}$ and $A_{50}^-B_{30}$ ($l_t = 80, r_b = 0.60, \varphi_p = 0.02, a_{AW} = 40$). Time evolution of complex-core size (number of beads A in the core) and radial distribution function (between the IgG1 and the polyelectrolyte block) for the systems with different r_b include (1) $l_t = 80, a_{AW} = 40$, and $\varphi_p = 0.05$, and (2) $l_t = 80, a_{AW} = 40$, and $\varphi_p = 0.04$. Radial distribution function between the IgG1 and the polyanion (and polycation) with different r_b and φ_p ($l_t = 80, a_{AW} = 40$). Time evolution formation of the system includes IgG1, $A_{55}^+B_{25}$ and $A_{55}^-B_{25}$ ($l_t = 80, r_b = 0.45, \varphi_p = 0.05, a_{AW} = 35$). Average contact between IgG1 beads and water beads and radial distribution function as functions of r_b and a_{AW} at a fixed polymer concentration $\varphi_p = 0.05$ and a fixed chain length $l_t = 80$. The time evolution of the number of aggregates (N_{agg}) at different simulation steps for different a_{AW} ($\varphi_p = 0.05, l_t = 80$, and $r_b = 0.78$). Time evolution of complex-core size (number of A beads in the core) for the systems with different l_t ($a_{AW} = 40, \varphi_p = 0.05, r_b = 1.67$). Radial distribution function between the IgG1 and water beads for the systems with, $a_{AW} = 40, \varphi_p = 0.05$, as a function of l_t and r_b . Radial distribution function between the IgG1 and the polyelectrolyte (bead type A) beads for the systems with different, $a_{AW} = 40, \varphi_p = 0.05$, as a function of l_t and r_b . Radial distribution function between the IgG1 and the polyanion (and polycation) for the systems with different l_t (40, 60, and 80), and (a) $r_b = 0.60, a_{AW} = 40$ and $\varphi_p = 0.05$.

The following files are available free of charge.

Supporting Information (PDF)

Author Affiliation

Corresponding Authors

Sousa Javan Nikkhah - Department of Physics, Bernal Institute, University of Limerick, V94 T9PX Limerick, Ireland; [Orcid.org/0000-0003-1725-4069](https://orcid.org/0000-0003-1725-4069); * Email: Sousa.Javannikkhah@ul.ie.

Damien Thompson - Department of Physics, Bernal Institute, University of Limerick, V94 T9PX Limerick, Ireland; [Orcid.org/0000-0003-2340-5441](https://orcid.org/0000-0003-2340-5441); * Email: Damien.Thompson@ul.ie.

Authors

Pierre-André Cazade - Department of Physics, Bernal Institute, University of Limerick, V94 T9PX Limerick, Ireland; [Orcid.org/0000-0002-6860-4658](https://orcid.org/0000-0002-6860-4658); Email: Pierre.Cazade@ul.ie.

Jennifer J. McManus - H. H Wills Physics Laboratory, University of Bristol, Bristol BS8 1TL, United Kingdom, [Orcid.org/0000-0003-3630-5108](https://orcid.org/0000-0003-3630-5108); Email: Jennifer.Mcmanus@bristol.ac.uk.

Author Contributions

The manuscript was written through contributions of all authors. All authors have given approval to the final version of the manuscript.

Funding Sources

The European Union's Horizon 2020 research and innovation programme under the Marie Skłodowska-Curie agreement no. 801165.

Science Foundation Ireland (SFI) under award 12/RC/2275_P2.

Notes

Any additional relevant notes should be placed here.

Acknowledgment

This work was supported by the European Union's Horizon 2020 research and innovation programme under the Marie Skłodowska-Curie grant to Sousa Javan Nikkhah, agreement no. 801165. Damien Thompson and Jennifer McManus acknowledge additional support from Science

Foundation Ireland (SFI) under award 12/RC/2275_P2, and Damien Thompson acknowledges also supercomputing resources at the SFI/Higher Education Authority Irish Center for High-End Computing (ICHEC).

Abbreviation

DPD Dissipative Particle Dynamics; LAMMPS large-scale Atomic-Molecular Massively Parallel Simulator.

References

- (1) Zhao, L.; Skwarczynski, M.; Toth, I. Polyelectrolyte-Based Platforms for the Delivery of Peptides and Proteins. *ACS Biomater. Sci. Eng.* **2019**, *5* (10), 4937–4950. <https://doi.org/10.1021/acsbio.1c01135>.
- (2) Lau, J. L.; Dunn, M. K. Therapeutic Peptides: Historical Perspectives, Current Development Trends, and Future Directions. *Bioorganic & Medicinal Chemistry* **2018**, *26* (10), 2700–2707. <https://doi.org/10.1016/j.bmc.2017.06.052>.
- (3) Craik, D. J.; Fairlie, D. P.; Liras, S.; Price, D. The Future of Peptide-Based Drugs. *Chemical Biology & Drug Design* **2013**, *81* (1), 136–147. <https://doi.org/10.1111/cbdd.12055>.
- (4) Kesik-Brodacka, M. Progress in Biopharmaceutical Development. *Biotechnol Appl Biochem* **2018**, *65* (3), 306–322. <https://doi.org/10.1002/bab.1617>.
- (5) Dimitrov, D. S. Therapeutic Proteins. *Methods Mol Biol* **2012**, *899*, 1–26. https://doi.org/10.1007/978-1-61779-921-1_1.
- (6) Gavin, A. L.; Huang, D.; Huber, C.; Mårtensson, A.; Tardif, V.; Skog, P. D.; Blane, T. R.; Thinnis, T. C.; Osborn, K.; Chong, H. S.; Kargaran, F.; Kimm, P.; Zeitjian, A.; Sielski, R. L.; Briggs, M.; Schulz, S. R.; Zarpellon, A.; Cravatt, B.; Pang, E. S.; Teijaro, J.; de la Torre, J. C.; O’Keeffe, M.; Hochrein, H.; Damme, M.; Teyton, L.; Lawson, B. R.; Nemazee, D. PLD3 and PLD4 Are Single-Stranded Acid Exonucleases That Regulate Endosomal Nucleic-Acid Sensing. *Nature Immunology* **2018**, *19* (9), 942–953. <https://doi.org/10.1038/s41590-018-0179-y>.
- (7) Sorolla, A.; Wang, E.; Golden, E.; Duffy, C.; Henriques, S. T.; Redfern, A. D.; Blancafort, P. Precision Medicine by Designer Interference Peptides: Applications in Oncology and Molecular Therapeutics. *Oncogene* **2020**, *39* (6), 1167–1184. <https://doi.org/10.1038/s41388-019-1056-3>.
- (8) Lee, A. C.-L.; Harris, J. L.; Khanna, K. K.; Hong, J.-H. A Comprehensive Review on Current Advances in Peptide Drug Development and Design. *Int J Mol Sci* **2019**, *20* (10). <https://doi.org/10.3390/ijms20102383>.
- (9) Du, A. W.; Stenzel, M. H. Drug Carriers for the Delivery of Therapeutic Peptides. *Biomacromolecules* **2014**, *15* (4), 1097–1114. <https://doi.org/10.1021/bm500169p>.
- (10) Padhi, A.; Sengupta, M.; Sengupta, S.; Roehm, K. H.; Sonawane, A. Antimicrobial Peptides and Proteins in Mycobacterial Therapy: Current Status and Future Prospects. *Tuberculosis* **2014**, *94* (4), 363–373. <https://doi.org/10.1016/j.tube.2014.03.011>.
- (11) Lagassé, H. A. D.; Alexaki, A.; Simhadri, V. L.; Katagiri, N. H.; Jankowski, W.; Sauna, Z. E.; Kimchi-Sarfaty, C. Recent Advances in (Therapeutic Protein) Drug Development. *F1000Res* **2017**, *6*. <https://doi.org/10.12688/f1000research.9970.1>.
- (12) Patra, J. K.; Das, G.; Fraceto, L. F.; Campos, E. V. R.; Rodriguez-Torres, M. del P.; Acosta-Torres, L. S.; Diaz-Torres, L. A.; Grillo, R.; Swamy, M. K.; Sharma, S.; Habtemariam, S.;

- Shin, H.-S. Nano Based Drug Delivery Systems: Recent Developments and Future Prospects. *J Nanobiotechnology* **2018**, *16*. <https://doi.org/10.1186/s12951-018-0392-8>.
- (13) Lee, Y.; Ishii, T.; Kim, H. J.; Nishiyama, N.; Hayakawa, Y.; Itaka, K.; Kataoka, K. Efficient Delivery of Bioactive Antibodies into the Cytoplasm of Living Cells by Charge-Conversional Polyion Complex Micelles. *Angewandte Chemie International Edition* **2010**, *49* (14), 2552–2555. <https://doi.org/10.1002/anie.200905264>.
 - (14) Khawli, L. A.; Biela, B. H.; Hu, P.; Epstein, A. L. Stable, Genetically Engineered F(Ab')₂ Fragments of Chimeric TNT-3 Expressed in Mammalian Cells. *Hybridoma and Hybridomics* **2002**, *21* (1), 11–18. <https://doi.org/10.1089/15368590252917593>.
 - (15) Boland, W. K.; Bebb, G. Nimotuzumab: A Novel Anti-EGFR Monoclonal Antibody That Retains Anti-EGFR Activity While Minimizing Skin Toxicity. *Expert Opinion on Biological Therapy* **2009**, *9* (9), 1199–1206. <https://doi.org/10.1517/14712590903110709>.
 - (16) Gemmete, J. J.; Mukherji, S. K. Trastuzumab (Herceptin): Fig 1. *AJNR Am J Neuroradiol* **2011**, *32* (8), 1373–1374. <https://doi.org/10.3174/ajnr.A2619>.
 - (17) Koury, J.; Lucero, M.; Cato, C.; Chang, L.; Geiger, J.; Henry, D.; Hernandez, J.; Hung, F.; Kaur, P.; Teskey, G.; Tran, A. Immunotherapies: Exploiting the Immune System for Cancer Treatment. *J Immunol Res* **2018**, *2018*. <https://doi.org/10.1155/2018/9585614>.
 - (18) Wootla, B.; Denic, A.; Rodriguez, M. Polyclonal and Monoclonal Antibodies in Clinic. In *Human Monoclonal Antibodies: Methods and Protocols*; Steinitz, M., Ed.; Methods in Molecular Biology; Humana Press: Totowa, NJ, 2014; pp 79–110. https://doi.org/10.1007/978-1-62703-586-6_5.
 - (19) Smaglo, B. G.; Aldeghaither, D.; Weiner, L. M. Antibody Therapy. In *Encyclopedia of Immunobiology*; Ratcliffe, M. J. H., Ed.; Academic Press: Oxford, 2016; pp 550–559. <https://doi.org/10.1016/B978-0-12-374279-7.17021-3>.
 - (20) Zahavi, D.; Weiner, L. Monoclonal Antibodies in Cancer Therapy. *Antibodies (Basel)* **2020**, *9* (3). <https://doi.org/10.3390/antib9030034>.
 - (21) Tsumoto, K.; Isozaki, Y.; Yagami, H.; Tomita, M. Future Perspectives of Therapeutic Monoclonal Antibodies. *Immunotherapy* **2019**, *11* (2), 119–127. <https://doi.org/10.2217/imt-2018-0130>.
 - (22) Baumann, A. Early Development of Therapeutic Biologics--Pharmacokinetics. *Curr Drug Metab* **2006**, *7* (1), 15–21. <https://doi.org/10.2174/138920006774832604>.
 - (23) Awwad, S.; Angkawinitwong, U. Overview of Antibody Drug Delivery. *Pharmaceutics* **2018**, *10* (3), 83. <https://doi.org/10.3390/pharmaceutics10030083>.
 - (24) Pereira de Sousa, I.; Bernkop-Schnürch, A. Pre-Systemic Metabolism of Orally Administered Drugs and Strategies to Overcome It. *J Control Release* **2014**, *192*, 301–309. <https://doi.org/10.1016/j.jconrel.2014.08.004>.
 - (25) Pisal, D. S.; Kosloski, M. P.; Balu-Iyer, S. V. DELIVERY OF THERAPEUTIC PROTEINS. *J Pharm Sci* **2010**, *99* (6), 2557–2575. <https://doi.org/10.1002/jps.22054>.
 - (26) Robertis, S. D.; Bonferoni, M. C.; Elviri, L.; Sandri, G.; Caramella, C.; Bettini, R. Advances in Oral Controlled Drug Delivery: The Role of Drug–Polymer and Interpolymer Non-Covalent Interactions. *Expert Opinion on Drug Delivery* **2015**, *12* (3), 441–453. <https://doi.org/10.1517/17425247.2015.966685>.
 - (27) Yin, L.; Yuvienco, C.; Montclare, J. K. Protein Based Therapeutic Delivery Agents: Contemporary Developments and Challenges. *Biomaterials* **2017**, *134*, 91–116. <https://doi.org/10.1016/j.biomaterials.2017.04.036>.

- (28) Insua, I.; Wilkinson, A.; Fernandez-Trillo, F. Polyion Complex (PIC) Particles: Preparation and Biomedical Applications. *European Polymer Journal* **2016**, *81*, 198–215. <https://doi.org/10.1016/j.eurpolymj.2016.06.003>.
- (29) Gao, S.; Holkar, A.; Srivastava, S. Protein–Polyelectrolyte Complexes and Micellar Assemblies. *Polymers* **2019**, *11* (7), 1097. <https://doi.org/10.3390/polym11071097>.
- (30) Jha, P. K.; Desai, P. S.; Li, J.; Larson, R. G. PH and Salt Effects on the Associative Phase Separation of Oppositely Charged Polyelectrolytes. *Polymers* **2014**, *6* (5), 1414–1436. <https://doi.org/10.3390/polym6051414>.
- (31) Lytle, T. K.; Chang, L.-W.; Markiewicz, N.; Perry, S. L.; Sing, C. E. Designing Electrostatic Interactions via Polyelectrolyte Monomer Sequence. *ACS Cent. Sci.* **2019**, *5* (4), 709–718. <https://doi.org/10.1021/acscentsci.9b00087>.
- (32) Potaś, J.; Szymańska, E.; Winnicka, K. Challenges in Developing of Chitosan – Based Polyelectrolyte Complexes as a Platform for Mucosal and Skin Drug Delivery. *European Polymer Journal* **2020**, *140*, 110020. <https://doi.org/10.1016/j.eurpolymj.2020.110020>.
- (33) Horn, J. M.; Kapelner, R. A.; Obermeyer, A. C. Macro- and Microphase Separated Protein–Polyelectrolyte Complexes: Design Parameters and Current Progress. *Polymers* **2019**, *11* (4), 578. <https://doi.org/10.3390/polym11040578>.
- (34) Semenyuk, P.; Muronetz, V. Protein Interaction with Charged Macromolecules: From Model Polymers to Unfolded Proteins and Post-Translational Modifications. *Int J Mol Sci* **2019**, *20* (5). <https://doi.org/10.3390/ijms20051252>.
- (35) Jiang, J.; Chen, E.-Q.; Yang, S. The Effect of Ion Pairs on Coacervate-Driven Self-Assembly of Block Polyelectrolytes. *J. Chem. Phys.* **2021**, *154* (14), 144903. <https://doi.org/10.1063/5.0044845>.
- (36) Voets, I. K.; de Keizer, A.; Cohen Stuart, M. A. Complex Coacervate Core Micelles. *Advances in Colloid and Interface Science* **2009**, *147–148*, 300–318. <https://doi.org/10.1016/j.cis.2008.09.012>.
- (37) Smolen, V. F.; Hagman, D. E. A Water Membrane Hypothesis: Behavior of Hydrated Polycation-Polyanion Salt Complexed Membranes as Apparent Lipoidal Barriers to Solute Transport. *Journal of Colloid and Interface Science* **1973**, *42* (1), 70–78. [https://doi.org/10.1016/0021-9797\(73\)90008-8](https://doi.org/10.1016/0021-9797(73)90008-8).
- (38) *Polyelectrolytes with Defined Molecular Architecture II*; Schmidt, M., Ed.; Advances in Polymer Science, Polyelectrolytes with Defined Molecular Architecture; Springer-Verlag: Berlin Heidelberg, 2004. <https://doi.org/10.1007/b10951>.
- (39) Laaser, J. E.; Jiang, Y.; Petersen, S. R.; Reineke, T. M.; Lodge, T. P. Interpolyelectrolyte Complexes of Polycationic Micelles and Linear Polyanions: Structural Stability and Temporal Evolution. *J. Phys. Chem. B* **2015**, *119* (52), 15919–15928. <https://doi.org/10.1021/acs.jpcc.5b09010>.
- (40) Takahashi, R.; Sato, T.; Terao, K.; Yusa, S. Reversible Vesicle–Spherical Micelle Transition in a Polyion Complex Micellar System Induced by Changing the Mixing Ratio of Copolymer Components. *Macromolecules* **2016**, *49* (8), 3091–3099. <https://doi.org/10.1021/acs.macromol.6b00308>.
- (41) Rumyantsev, A. M.; Zhulina, E. B.; Borisov, O. V. Scaling Theory of Complex Coacervate Core Micelles. *ACS Macro Lett.* **2018**, *7* (7), 811–816. <https://doi.org/10.1021/acsmacrolett.8b00316>.
- (42) Takahashi, R.; Narayanan, T.; Yusa, S.; Sato, T. Kinetics of Morphological Transition between Cylindrical and Spherical Micelles in a Mixture of Anionic–Neutral and Cationic–

- Neutral Block Copolymers Studied by Time-Resolved SAXS and USAXS. *Macromolecules* **2018**, *51* (10), 3654–3662. <https://doi.org/10.1021/acs.macromol.8b00101>.
- (43) Kwolek, U.; Nakai, K.; Pluta, A.; Zatorska, M.; Wnuk, D.; Lasota, S.; Bednar, J.; Michalik, M.; Yusa, S.; Kepczynski, M. Polyion Complex Vesicles (PICsomes) from Strong Copolyelectrolytes. Stability and in Vitro Studies. *Colloids and Surfaces B: Biointerfaces* **2017**, *158*, 658–666. <https://doi.org/10.1016/j.colsurfb.2017.07.042>.
- (44) Hori, M.; Cabral, H.; Toh, K.; Kishimura, A.; Kataoka, K. Robust Polyion Complex Vesicles (PICsomes) under Physiological Conditions Reinforced by Multiple Hydrogen Bond Formation Derived by Guanidinium Groups. *Biomacromolecules* **2018**, *19* (10), 4113–4121. <https://doi.org/10.1021/acs.biomac.8b01097>.
- (45) Fan, Y.; Tang, S.; Thomas, E. L.; Olsen, B. D. Responsive Block Copolymer Photonics Triggered by Protein–Polyelectrolyte Coacervation. *ACS Nano* **2014**, *8* (11), 11467–11473. <https://doi.org/10.1021/nn504565r>.
- (46) Wibowo, A.; Osada, K.; Matsuda, H.; Anraku, Y.; Hirose, H.; Kishimura, A.; Kataoka, K. Morphology Control in Water of Polyion Complex Nanoarchitectures of Double-Hydrophilic Charged Block Copolymers through Composition Tuning and Thermal Treatment. *Macromolecules* **2014**, *47* (9), 3086–3092. <https://doi.org/10.1021/ma500314d>.
- (47) Il'ina, A. V.; Varlamov, V. P. Chitosan-Based Polyelectrolyte Complexes: A Review. *Appl Biochem Microbiol* **2005**, *41* (1), 5–11. <https://doi.org/10.1007/s10438-005-0002-z>.
- (48) Katayose, S.; Kataoka, K. Remarkable Increase in Nuclease Resistance of Plasmid DNA through Supramolecular Assembly with Poly(Ethylene Glycol)–Poly(L-Lysine) Block Copolymer. *Journal of Pharmaceutical Sciences* **1998**, *87* (2), 160–163. <https://doi.org/10.1021/js970304s>.
- (49) Miyata, K.; Christie, R. J.; Kataoka, K. Polymeric Micelles for Nano-Scale Drug Delivery. *Reactive and Functional Polymers* **2011**, *71* (3), 227–234. <https://doi.org/10.1016/j.reactfunctpolym.2010.10.009>.
- (50) Harada, A.; Kataoka, K. Chain Length Recognition: Core-Shell Supramolecular Assembly from Oppositely Charged Block Copolymers. *Science* **1999**, *283* (5398), 65–67. <https://doi.org/10.1126/science.283.5398.65>.
- (51) Cabral, H.; Miyata, K.; Osada, K.; Kataoka, K. Block Copolymer Micelles in Nanomedicine Applications. *Chem. Rev.* **2018**, *118* (14), 6844–6892. <https://doi.org/10.1021/acs.chemrev.8b00199>.
- (52) Pippa, N.; Demetzos, S. P. and C. Polymer Self-Assembled Nanostructures as Innovative Drug Nanocarrier Platforms <https://www.eurekaselect.com/139597/article> (accessed 2021 - 01 -06).
- (53) Chen, F.; Stenzel, M. H. Polyion Complex Micelles for Protein Delivery. *Aust. J. Chem.* **2018**, *71* (10), 768. <https://doi.org/10.1071/CH18219>.
- (54) Hoogerbrugge, P. J.; Koelman, J. M. V. A. Simulating Microscopic Hydrodynamic Phenomena with Dissipative Particle Dynamics. *EPL* **1992**, *19* (3), 155–160. <https://doi.org/10.1209/0295-5075/19/3/001>.
- (55) Español, P.; Warren, P. Statistical Mechanics of Dissipative Particle Dynamics. *EPL* **1995**, *30* (4), 191–196. <https://doi.org/10.1209/0295-5075/30/4/001>.
- (56) Groot, R. D.; Warren, P. B. Dissipative Particle Dynamics: Bridging the Gap between Atomistic and Mesoscopic Simulation. *J. Chem. Phys.* **1997**, *107* (11), 4423–4435. <https://doi.org/10.1063/1.474784>.

- (57) Fiszman, G. L.; Jasnis, M. A. Molecular Mechanisms of Trastuzumab Resistance in HER2 Overexpressing Breast Cancer. *International Journal of Breast Cancer* **2011**, *2011*, 352182. <https://doi.org/10.4061/2011/352182>.
- (58) Hermanto, S.; Yusuf, M.; Mutalib, A.; Hudiyono, S. Molecular Dynamic Simulation of Trastuzumab F(Ab')₂ Structure in Corporation with HER2 as a Theranostic Agent of Breast Cancer. *J. Phys.: Conf. Ser.* **2017**, *835*, 012005. <https://doi.org/10.1088/1742-6596/835/1/012005>.
- (59) Pohlmann, P. R.; Mayer, I. A.; Mernaugh, R. Resistance to Trastuzumab in Breast Cancer. *Clin Cancer Res* **2009**, *15* (24), 7479–7491. <https://doi.org/10.1158/1078-0432.CCR-09-0636>.
- (60) Goswami, M.; Sumpter, B. G.; Huang, T.; Messman, J. M.; Gido, S. P.; Isaacs-Sodeye, A. I.; Mays, J. W. Tunable Morphologies from Charged Block Copolymers. *Soft Matter* **2010**, *6* (24), 6146–6154. <https://doi.org/10.1039/C0SM00733A>.
- (61) Wang, X.; Goswami, M.; Kumar, R.; Sumpter, B. G.; Mays, J. Morphologies of Block Copolymers Composed of Charged and Neutral Blocks. *Soft Matter* **2012**, *8* (11), 3036–3052. <https://doi.org/10.1039/C2SM07223H>.
- (62) Borreguero, J. M.; Pincus, P. A.; Sumpter, B. G.; Goswami, M. Unraveling the Agglomeration Mechanism in Charged Block Copolymer and Surfactant Complexes. *Macromolecules* **2017**, *50* (3), 1193–1205. <https://doi.org/10.1021/acs.macromol.6b02319>.
- (63) Borreguero, J. M.; Pincus, P. A.; Sumpter, B. G.; Goswami, M. Dynamics of Charged Species in Ionic-Neutral Block Copolymer and Surfactant Complexes. *J. Phys. Chem. B* **2017**, *121* (28), 6958–6968. <https://doi.org/10.1021/acs.jpcc.7b05047>.
- (64) Dandekar, R.; Ardekani, A. M. Monoclonal Antibody Aggregation near Silicone Oil–Water Interfaces. *Langmuir* **2021**, *37* (4), 1386–1398. <https://doi.org/10.1021/acs.langmuir.0c02785>.
- (65) Chaudhri, A.; Zarraga, I. E.; Kamerzell, T. J.; Brandt, J. P.; Patapoff, T. W.; Shire, S. J.; Voth, G. A. Coarse-Grained Modeling of the Self-Association of Therapeutic Monoclonal Antibodies. *J. Phys. Chem. B* **2012**, *116* (28), 8045–8057. <https://doi.org/10.1021/jp301140u>.
- (66) Brandt, J. P.; Patapoff, T. W.; Aragon, S. R. Construction, MD Simulation, and Hydrodynamic Validation of an All-Atom Model of a Monoclonal IgG Antibody. *Biophys J* **2010**, *99* (3), 905–913. <https://doi.org/10.1016/j.bpj.2010.05.003>.
- (67) Šindelka, K.; Limpouchová, Z.; Lísal, M.; Procházka, K. Dissipative Particle Dynamics Study of Electrostatic Self-Assembly in Aqueous Mixtures of Copolymers Containing One Neutral Water-Soluble Block and One Either Positively or Negatively Charged Polyelectrolyte Block. *Macromolecules* **2014**, *47* (17), 6121–6134. <https://doi.org/10.1021/ma501018x>.
- (68) Posel, Z.; Limpouchová, Z.; Šindelka, K.; Lísal, M.; Procházka, K. Dissipative Particle Dynamics Study of the PH-Dependent Behavior of Poly(2-Vinylpyridine)-Block-Poly(Ethylene Oxide) Diblock Copolymer in Aqueous Buffers. *Macromolecules* **2014**, *47* (7), 2503–2514. <https://doi.org/10.1021/ma402293c>.
- (69) Wang, X.; Gao, J.; Wang, Z.; Xu, J.; Li, C.; Sun, S.; Hu, S. Dissipative Particle Dynamics Simulation on the Self-Assembly and Disassembly of PH-Sensitive Polymeric Micelle with Coating Repair Agent. *Chemical Physics Letters* **2017**, *685*, 328–337. <https://doi.org/10.1016/j.cplett.2017.07.070>.

- (70) Seaton, M. A.; Anderson, R. L.; Metz, S.; Smith, W. DL_MESO: Highly Scalable Mesoscale Simulations. *Molecular Simulation* **2013**, *39* (10), 796–821. <https://doi.org/10.1080/08927022.2013.772297>.
- (71) Plimpton, S. Fast Parallel Algorithms for Short-Range Molecular Dynamics. *Journal of Computational Physics* **1995**, *117* (1), 1–19. <https://doi.org/10.1006/jcph.1995.1039>.
- (72) Humphrey, W.; Dalke, A.; Schulten, K. VMD: Visual Molecular Dynamics. *Journal of Molecular Graphics* **1996**, *14* (1), 33–38. [https://doi.org/10.1016/0263-7855\(96\)00018-5](https://doi.org/10.1016/0263-7855(96)00018-5).
- (73) Shen, Z.; Ye, H.; Kröger, M.; Li, Y. Self-Assembled Core–Polyethylene Glycol–Lipid Shell Nanoparticles Demonstrate High Stability in Shear Flow. *Phys. Chem. Chem. Phys.* **2017**, *19* (20), 13294–13306. <https://doi.org/10.1039/C7CP01530E>.
- (74) Wang, Y.; Li, B.; Zhou, Y.; Lu, Z.; Yan, D. Dissipative Particle Dynamics Simulation Study on the Mechanisms of Self-Assembly of Large Multimolecular Micelles from Amphiphilic Dendritic Multiarm Copolymers. *Soft Matter* **2013**, *9* (12), 3293–3304. <https://doi.org/10.1039/C3SM27396B>.
- (75) Šindelka, K.; Limpouchová, Z.; Lísal, M.; Procházka, K. The Electrostatic Co-Assembly in Non-Stoichiometric Aqueous Mixtures of Copolymers Composed of One Neutral Water-Soluble and One Polyelectrolyte (Either Positively or Negatively Charged) Block: A Dissipative Particle Dynamics Study. *Phys. Chem. Chem. Phys.* **2016**, *18* (24), 16137–16151. <https://doi.org/10.1039/C6CP01047D>.
- (76) Wang, Y.; Li, Q. Y.; Liu, X. B.; Zhang, C. Y.; Wu, Z. M.; Guo, X. D. Mesoscale Simulations and Experimental Studies of PH-Sensitive Micelles for Controlled Drug Delivery. *ACS Appl. Mater. Interfaces* **2015**, *7* (46), 25592–25600. <https://doi.org/10.1021/acsami.5b08366>.
- (77) Šindelka, K.; Limpouchová, Z.; Procházka, K. Computer Study of the Solubilization of Polymer Chains in Polyelectrolyte Complex Cores of Polymeric Nanoparticles in Aqueous Media. *Physical Chemistry Chemical Physics* **2018**, *20* (47), 29876–29888. <https://doi.org/10.1039/C8CP05907A>.
- (78) Sadman, K.; Wang, Q.; Chen, Y.; Keshavarz, B.; Jiang, Z.; Shull, K. R. Influence of Hydrophobicity on Polyelectrolyte Complexation. *Macromolecules* **2017**, *50* (23), 9417–9426. <https://doi.org/10.1021/acs.macromol.7b02031>.
- (79) Sofronova, A.; Semenyuk, P.; Muronetz, V. The Influence of β -Casein Glycation on Its Interaction with Natural and Synthetic Polyelectrolytes. *Food Hydrocolloids* **2019**, *89*, 425–433. <https://doi.org/10.1016/j.foodhyd.2018.11.011>.
- (80) Ou, Z.; Muthukumar, M. Entropy and Enthalpy of Polyelectrolyte Complexation: Langevin Dynamics Simulations. *J. Chem. Phys.* **2006**, *124* (15), 154902. <https://doi.org/10.1063/1.2178803>.
- (81) Šindelka, K.; Limpouchová, Z.; Lísal, M.; Procházka, K. Dissipative Particle Dynamics Study of Electrostatic Self-Assembly in Aqueous Mixtures of Copolymers Containing One Neutral Water-Soluble Block and One Either Positively or Negatively Charged Polyelectrolyte Block. *Macromolecules* **2014**, *47* (17), 6121–6134. <https://doi.org/10.1021/ma501018x>.
- (82) Nagarajan, R.; Barry, M.; Ruckenstein, E. Unusual Selectivity in Solubilization by Block Copolymer Micelles. *Langmuir* **1986**, *2* (2), 210–215. <https://doi.org/10.1021/la00068a017>.
- (83) Hpone Myint, K.; Brown, J. R.; Shim, A. R.; Wyslouzil, B. E.; Hall, L. M. Encapsulation of Nanoparticles During Polymer Micelle Formation: A Dissipative Particle Dynamics

- Study. *J. Phys. Chem. B* **2016**, *120* (44), 11582–11594. <https://doi.org/10.1021/acs.jpcc.6b07324>.
- (84) Gummel, J.; Cousin, F.; Boué, F. Counterions Release from Electrostatic Complexes of Polyelectrolytes and Proteins of Opposite Charge: A Direct Measurement. *J. Am. Chem. Soc.* **2007**, *129* (18), 5806–5807. <https://doi.org/10.1021/ja070414t>.
- (85) Aberkane, L.; Jasniewski, J.; Gaiani, C.; Scher, J.; Sanchez, C. Thermodynamic Characterization of Acacia Gum- β -Lactoglobulin Complex Coacervation. *Langmuir* **2010**, *26* (15), 12523–12533. <https://doi.org/10.1021/la100705d>.
- (86) Priftis, D.; Megley, K.; Laugel, N.; Tirrell, M. Complex Coacervation of Poly(Ethylene-Imine)/Polypeptide Aqueous Solutions: Thermodynamic and Rheological Characterization. *J Colloid Interface Sci* **2013**, *398*, 39–50. <https://doi.org/10.1016/j.jcis.2013.01.055>.
- (87) Rathee, V. S.; Sidky, H.; Sikora, B. J.; Whitmer, J. K. Role of Associative Charging in the Entropy–Energy Balance of Polyelectrolyte Complexes. *J. Am. Chem. Soc.* **2018**, *140* (45), 15319–15328. <https://doi.org/10.1021/jacs.8b08649>.
- (88) Elder, R. M.; Emrick, T.; Jayaraman, A. Understanding the Effect of Polylysine Architecture on DNA Binding Using Molecular Dynamics Simulations. *Biomacromolecules* **2011**, *12* (11), 3870–3879. <https://doi.org/10.1021/bm201113y>.
- (89) Nyquist, R. M.; Ha, B.-Y.; Liu, A. J. Counterion Condensation in Solutions of Rigid Polyelectrolytes. *Macromolecules* **1999**, *32* (10), 3481–3487. <https://doi.org/10.1021/ma9811021>.